Block Tectonics Across Western Tibet and Multi-Millennial Recurrence of Great Earthquakes on the Karakax Fault

H. Li, M. Chevalier, P. Tapponnier, J. Pan, Jerome van Der Woerd, A. Mériaux, F. Ryerson, G. Peltzer, Z. Sun, J. Si, et al.

Block Tectonics across Western Tibet and Multi-Millennial Recurrence of Great Earthquakes on the Karakax Fault

H. Li[1,2*], M.L. Chevalier[1,2], P. Tapponnier[3,2], J. Pan[1,2], J. Van der Woerd[4], A.S. Mériaux[4], F.J. Ryerson[5], G. Peltzer[6,7], Z. Sun[8], J. Si[1,2], J. Pei[8], and X. Xu[3]

[1] Key Laboratory of Deep-Earth Dynamics of Ministry of Natural Resources, Institute of Geology, Chinese Academy of Geological Sciences, Beijing, China
[2] Southern Marine Science and Engineering Guangdong Laboratory (Guangzhou), Guangzhou, China
[3] National Institute of Natural Hazards, Ministry of Emergency Management of China, Beijing, China
[4] Institut Terre et Environnement de Strasbourg, Strasbourg, France
[5] Lawrence Livermore National Laboratory, Livermore, California, USA
[6] University of California Los Angeles, Los Angeles, CA95095, USA
[7] Jet Propulsion Laboratory, California Institute of Technology, CA, USA
[8] Institute of Geomechanics, Chinese Academy of Geological Sciences, Beijing, China

Corresponding author: Haibing Li (lihaibing06@163.com)

Key Points:

- The ~400 km-long, left-lateral Karakax fault (western Altyn Tagh fault) slip rate has been ~2.5±0.5 mm/yr for ~210 ka
- Four M~7.6 earthquakes (150 km rupture length; 2.5 ka return time) have offset Holocene terraces (6, 12, 18 and 24 m characteristic slip)

26 • Block tectonics and triple junction kinematics account for 24 Ma deformation of west
27 Tibet and rise of ≥8000 m-high Karakorum range

28

Abstract

Fault slip rates are critical to quantify continental deformation. Those along the Karakax fault (northwestern Altyn Tagh Fault: ATF) have been debated, even though it is one of Tibet's most outstanding active faults. At Taersa, using LiDAR measurements of terrace and fan riser offsets (~6 to ~500 m) and $^{10}Be/^{26}Al$ dating of alluvial surfaces (<210 ka), we obtain a late Quaternary slip rate of ~2.5±0.5 mm/yr. This doubles the ~2.6±0.5 mm/yr rate time span found to the east and west. We interpret the ~150 km-long, free-faced rupture along the fault to be that of the M~7.6 event felt in Hotan in 1882. Characteristic slip (~6 m) during four large earthquakes since ~10 ka implies a ~2500±500 yrs return time. A ~3 mm/yr rate is consistent with the ~80 km offset of the Karakax river since uplift of the West Kunlun range and sediment deposition in the Tarim foreland accelerated, ~24 Ma ago. The faster slip rate (~10.5 mm/yr) on the central ATF matches the sum of those along the reactivated West Tibetan terrane boundaries (Karakax and Longmu-Gozha Co faults) at the Uzatagh triple junction (~36°N, 83°E). The abrupt termination and altitude drop of the Karakorum range where the Longmu Co and Karakorum faults meet (Angmong junction), also reflect triple junction kinematics. Such localized changes account for the rise of the Karakorum and West Kunlun ranges and support lithospheric block tectonics rather than diffusely distributed deformation.

Plain Language Summary

How the Tibetan plateau rose to ~4500 m and deforms today remain outstanding questions. Tibet's northern edge follows the ~2000 km-long Altyn Tagh fault, whose westernmost branch is the Karakax fault. Despite the spectacular escarpments and offsets

observed along that fault, its slip rate, critical to quantify continental deformation, has remained controversial. Here, we corroborate that, for the last ~210,000 yrs, that rate has been ~2.5±0.5 mm/yr, based on high-resolution topography and dating of left-laterally offset fluvial surfaces. The ~80 km offset of the Karakax river implies that this rate may have remained constant since the rise of the Kunlun range above the Tarim basin started ~24 Ma ago. The sharp fault trace reflects the exceptional preservation, since ~10,000 years ago, of four M~7.6 earthquake ruptures (the last in 1882), each with ~6 m of slip (~2500 yrs return time). Fault slip rates, GPS vectors and mountain altitudes across western Tibet reflect block motions and triple junction kinematics rather than continuum deformation. Specifically, localized velocity changes appear to account for the rise of the West Kunlun and Karakorum ranges. Our results bridge the gaps between present and long-term geological history, and broad-scale geodesy and local field evidence.

1 Introduction

The accurate determination of fault slip rates at various timescales is key to quantifying continental deformation kinematics, long-term seismicity and lithospheric rheology. Yet, because fault offsets and marker ages derived from different measurements and dating techniques are often difficult to constrain beyond doubt or to interpret jointly, and because slip-rates can be time-dependent (e.g., Chevalier et al., 2005), conflicting long-term slip rate values have been proposed along even the best studied active faults. In western Tibet, the longest segment of the ~400 km-long, ~100°E-striking Karakax fault (KXF), northwestern branch of the ~2000 km-long, left-lateral Altyn Tagh fault (ATF), is partly confined along the ~3-4 km-wide Karakax river valley. It follows the southern edge of the West Kunlun range, along the northern boundary of the Tianshuihai terrane (Fig. 1). Together with the sinistral Longmu-Gozha Co and dextral

74 Karakorum faults farther south, it contributes to absorb the convergence between India and Asia,
75 and to steer the eastward extrusion of Tibet (e.g., Tapponnier and Molnar, 1977; Armijo et al.,
76 1989; Avouac and Tapponnier, 1993; Tapponnier et al., 2001; Chevalier et al., 2017). Due to
77 access restrictions and a remote location at ~3700 m, the KXF has been the target of few field
78 studies (e.g., Matte et al., 1996; Li et al., 2012; Gong et al., 2017; Peltzer et al., 2020), in spite of
79 spectacular, long-identified geomorphic markers (pull-apart basins, pressure ridges, and offset
80 streams, terraces, fans and moraines) (Peltzer et al., 1989).

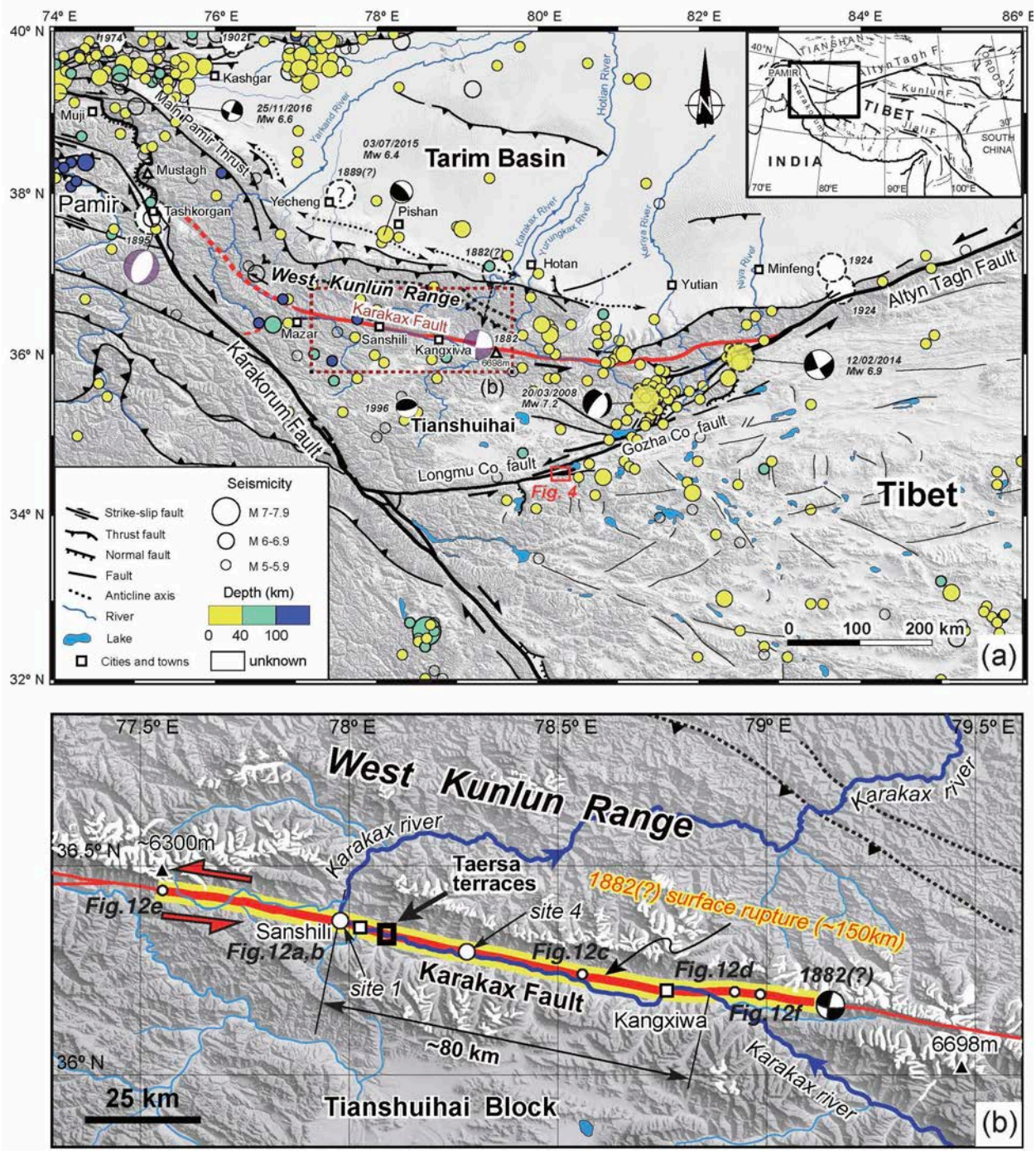

Figure 1. *Active faulting in the Altyn Tagh - Karakorum junction area. (a) Simplified map of Quaternary faults across western Tibet and Tarim (Karakax fault in red). Inset shows location within India-Asia collision zone. Circles are epicenters of M≥5 earthquakes since 1976 (SBX, 1997; USGS), colored as a function of depth. Dashed large white circles are reported or inferred locations of older historical earthquakes. Black/white fault plane solutions are for M≥6.4*

earthquakes recorded by www.globalcmt.org, while two light-purple/white ones are those of the 1882 and 1895 historical events, consistent with surface rupture observations (Liu, 1993). (b) Close-up of left-lateral Karakax fault main trace. Black square is location of Taersa terraces site. Thick yellow/red line shows ~150 km length of inferred sinistral surface rupture of 1882 earthquake (black/white focal mechanism). Note ~80 km sinistral offset of Karakax river. Large white circles are Sites 1 and 4 from Peltzer et al. (2020) and small white circles refer to surface rupture field photographs and satellite images shown in Figure 12.

Pioneering observations with Landsat images demonstrated that the KXF is an active left-lateral strike-slip fault (Tapponnier and Molnar, 1977). The subsequent use of 10 m-resolution Spot images provided the first measurements of syn- or post-glacial offsets of up to 250 m (Peltzer et al., 1989). This initially suggested an inferred Holocene slip rate as large as ~20-24 mm/yr, in keeping with the youthful geomorphic trace of the fault. Such a fast rate similar to that along California's San Andreas fault and compatible with that formerly inferred along the central ATF (~30 mm/yr, e.g., Molnar et al., 1987; Armijo et al., 1989; Molnar and Lyon-Caen, 1989) was long deemed plausible (e.g., Avouac and Peltzer, 1993; Avouac and Tapponnier, 1993). This was also consistent with a convergence rate between India and Asia formerly estimated to be as large as ~5 cm/yr based on Nuvel 1 and plate tectonic reconstructions (DeMets et al., 1990). Later on, quantitative field measurements and sampling suggested a slip rate bracket of 12-25 mm/yr in the last ~115 ka (Ryerson et al., 1999; dataset published in Peltzer et al., 2020). Much slower slip rates, however, have been proposed in recent years. Li et al. (2012) suggested ~6-7 mm/yr during the last ~1000 years, based on one ^{14}C age in a trench ~2 km east of Sanshili (Fig. 2). At the location of our present study, from Optically Stimulated Luminescence (OSL) dating of fluvial sand samples from offset river terraces, Gong et al. (2017) obtained a similar rate of 7.8±1.6 mm/yr during the last ~40 ka. Yet more recently, Peltzer et al. (2020) obtained an even

112 slower rate of 2.6±0.5 mm/yr since ~115 ka, by combining diffusion modeling of fault scarps,
113 3D fan offset reconstructions, and OSL/^{10}Be dating of offset terraces at two sites ~35 km apart
114 (Fig. 1b).

115 Here, based on Light Detection And Ranging (LiDAR) geomorphic measurements and
116 ^{10}Be/^{26}Al cosmogenic surface-exposure and depth profile dating at Taersa, 5 km east of Sanshili,
117 we further assess plausible values of the KXF slip rate in the last ~210 ka and infer the return
118 times of four Holocene great earthquakes on the fault. This is possible because of the outstanding
119 preservation of superficial morphology due to a particularly arid climate (36 mm/yr of annual
120 precipitation in Kangxiwa, Yao et al., 1996). We also re-assess the ~150 ka slip rate along the
121 Longmu Co fault, ~250 km SE of the Karakax valley, and examine how such large faults control
122 the large-scale kinematics of block deformation across western Tibet.

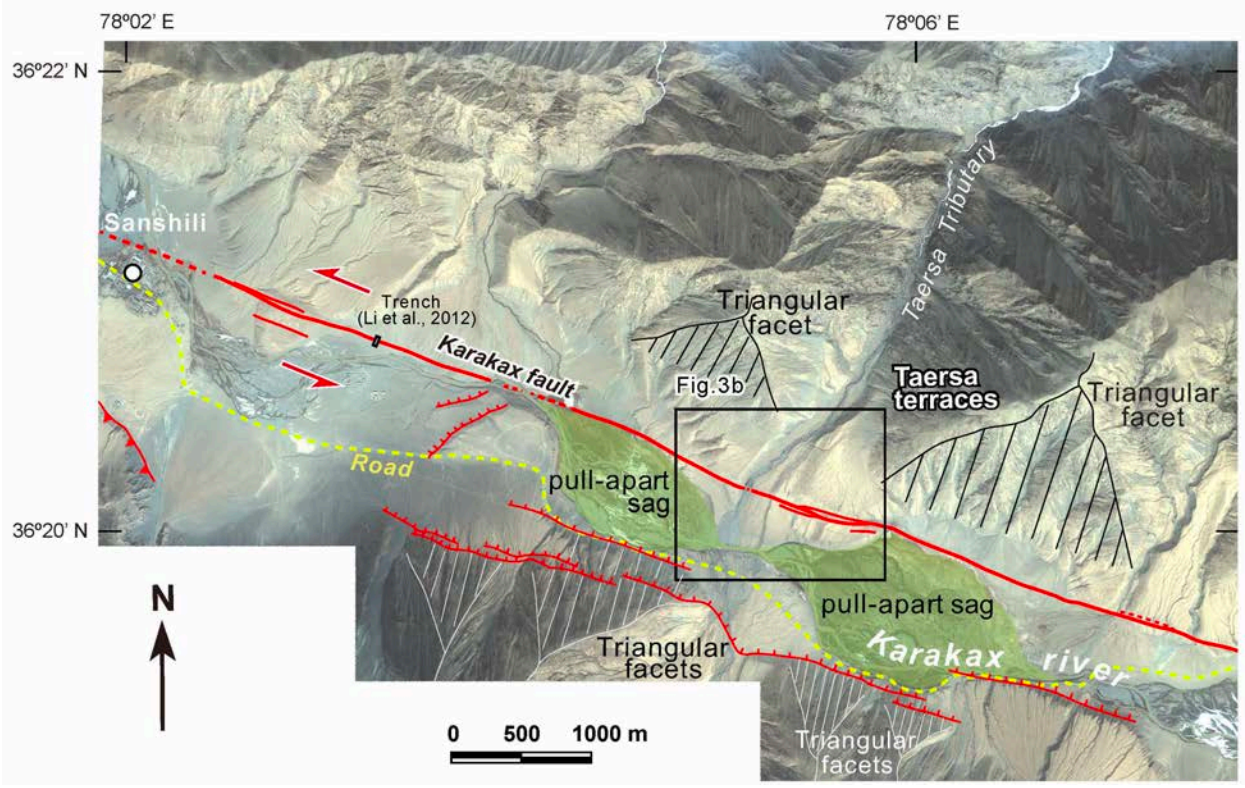

123

124 ***Figure 2.*** *Map of main active strands of Karakax fault system around Taersa site, based on*
125 *Ikonos image and field mapping of recent surface traces (red) across Karakax valley near*

Sanshili. The Taersa tributary flows south into a deep, swampy pull-apart sag (green shade) along the river valley, abandoning uplifted fans and terraces across the fault. Recent, north-facing and NE-striking normal fault scarps (red lines with tick bars) also cut fluvial fans south of the river. Triangular facets attesting to components of normal faulting south and north of the river are also indicated. Black rectangle shows location of trench site from Li et al. (2012).

2 Methods

Meltwaters from the West Kunlun range glaciers flow into the ~EW-trending Karakax river valley (Fig. 2), depositing large fans and terraces (Fig. 3). The Karakax strike-slip fault, which runs parallel to the Karakax river, cuts and left-laterally displaces by tens to hundreds of meters most of these tributary landforms (Figs. 2 and 3). This ideal setting creates piercing points on each side of the fault that can be used to measure offsets, with assessable uncertainties thanks to the fairly linear geometry of the terrace risers.

We combined field measurements and high-resolution satellite image interpretation to map active fault strands and offset geomorphic features, particularly within the Taersa paleo-fans and inset terraces (Fig. 3). In the field, using a tape, we first measured horizontal strike-slip offsets smaller than 30 m. We also used a Riegl VZ-1000 terrestrial LiDAR (angular resolution of 0.02° for raw data) to scan the Taersa fan and fan/terrace surfaces (five bases, Fig. 3b,d). After generating the point cloud using Riegl's "RiscanPro" software, we exported the data into "Global Mapper" to build a Digital Elevation Model (DEM) with a resolution of 0.5 m. We then extracted topographic profiles from the DEM and precisely measured cumulative horizontal and vertical fault offsets (Fig. 5). All DEM-derived measurements were compared with those directly measured in the field. Our high-resolution DEM, combined with the Ikonos satellite image of the entire Taersa site, was finally used to quantify the overall geometry of the fans and their offsets by the KXF (Figs. 5 and 6b).

151 At a more detailed level, we used the Matlab code "3D_Fault_Offsets" of Stewart et al.
152 (2018) to measure the horizontal and vertical offsets of the youngest terrace risers (T0, T0', T0"
153 and T2) (Figs. S1-S4). That code requires tracing of the fault on the DEM and identifying
154 polygons to delineate terrace risers on both sides of the fault. Channel meandering along the
155 various risers requires reducing the width of the polygons. The DEM uncertainties were set to be
156 0.5 m, and 2 m for the position of the fault whose dip was taken to be 70±10° (from trenching by
157 Li et al., 2012).
158 We also show in Figure 4 the DEM (9.78 cm/pix) that we recently obtained across the
159 Longmu Co fault, where it offsets the highest shoreline of Sumxi-Longmu Lake (location in Fig.
160 1a). That DEM was built by merging dozens of photos taken by our Unmanned Aerial Vehicle
161 (UAV, DJI Phantom 4) using the software "Agisoft Metashape Professional".
162 Our dating of fans and terraces at Taersa was based on the collection of a total of 35 quartz-
163 rich cobbles (<25 cm in diameter) on the surfaces, as well as of nine samples in two depth
164 profiles (down to ~140 cm) (Figs. 3, 8 and S5). From these samples, we obtained 35 ^{10}Be and six
165 ^{26}Al cosmogenic model ages (Table 1). The clear desert varnish coating all the cobble surfaces
166 (Figs. 8 and S5) (Farr and Chadwick, 1996), including on the lowest, youngest terraces, strongly
167 suggests an absence of post-depositional reworking, and minimal rock weathering. The cobbles
168 were crushed and sieved, and mineral separation and quartz cleaning were performed following
169 standard procedures (e.g., Kohl and Nishiizumi, 1992). ^{10}Be and ^{26}Al model ages were calculated
170 using the Lifton et al. (2014) 'LSDn' model in CRONUS version 3 (Balco et al., 2008) and are
171 reported with 1σ uncertainties (Table 1). The model ages from the two depth profiles were
172 calculated using the Hidy et al. (2010) software (version 1.2).

173 We used statistical analyses based on Chauvenet's criterion (Bevington and Robinson, 2002)
174 to discard potential outliers (including samples with excessive or insufficient ^{10}Be or ^{26}Al
175 concentrations) out of the age distributions. Slip rates during different time spans were then
176 derived from the ranges of fan and terrace riser offsets and abandonment ages using the method
177 of Zechar and Frankel (2009). We report the median rates (with uncertainties at the 68.27%
178 confidence interval about the median) obtained using their Gaussian uncertainty model.
179

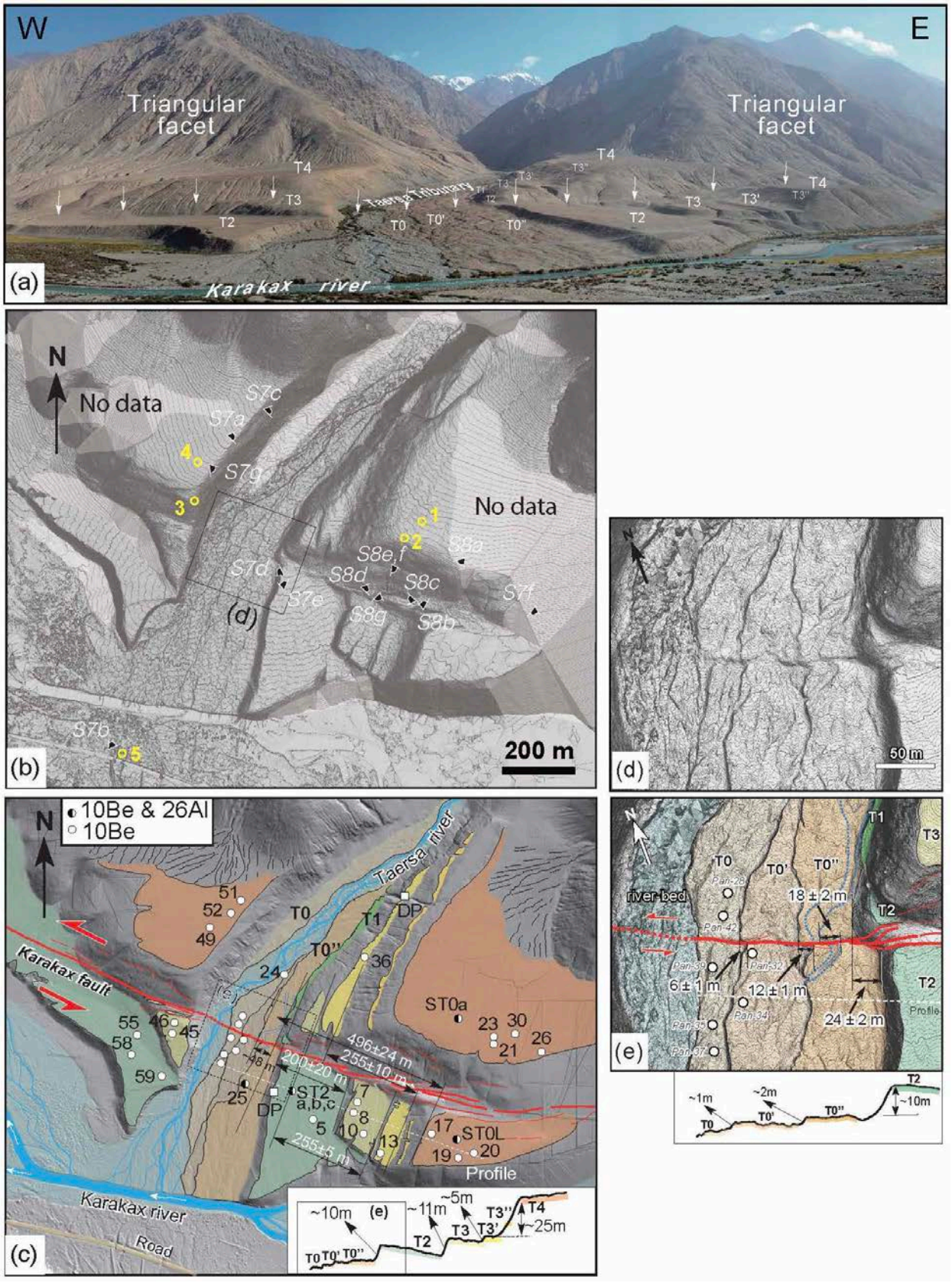
W
E
Triangular facet
Triangular facet
T4
T3
T2
T0
T0'
T0"
T3'
T3"
Taersa tributary
Karakax river
(a)
N
No data
No data
S7c
S7a
S7g
S8e,f
S8a
S7d
S8d
S8c
S7f
S7e
S8g
S8b
S7b
(d)
200 m
(b)
50 m
(d)
10Be & 26Al
10Be
Taersa river
Karakax fault
Karakax river
Road
ST0a
ST2 a,b,c
ST0L
DP
Profile
496±24 m
255±10 m
200±20 m
255±5 m
(c)
river bed
18 ± 2 m
6 ± 1 m
12 ± 1 m
24 ± 2 m
Profile
(e)
~10m
~11m
~5m
~25m
~1m
~2m
~10m

180

Figure 3. *Taersa terraces site: (a) View to NE of offset Taersa terraces and triangular facets. White arrows indicate main surface trace of Karakax fault. Note similar, maximum elevations of highest T4 fan surfaces on either side of the Taersa tributary valley. Location of photos in Figures S7 and S8 is indicated. (b and d) LiDAR DEM images (with 1 and 0.2 m contour lines, respectively), with (c and e) detailed field-based mapping of T0-T4 alluvial surfaces (colored) and seismic offsets, respectively. White areas in b are shielded from LiDAR surveys and five yellow circles show positions of survey bases. Small white circles (with numbers) indicate locations of dated cosmogenic surface samples. White squares labeled 'DP' are locations of depth profiles on T3' north of the fault and T2 south of the fault. Double arrows with numbers (in c) are apparent offsets of T4-T3'-T3 fan risers east of Taersa Holocene T0''/T0' fluvial channel (see text for details). Bottom right insets show profiles parallel to the fault (white dashed lines in c and e) across alluvial surfaces, extracted from LiDAR DEM. Single arrows with numbers (in e) point to single and cumulative co-seismic offsets of lowest T0 to T2 terrace risers.*

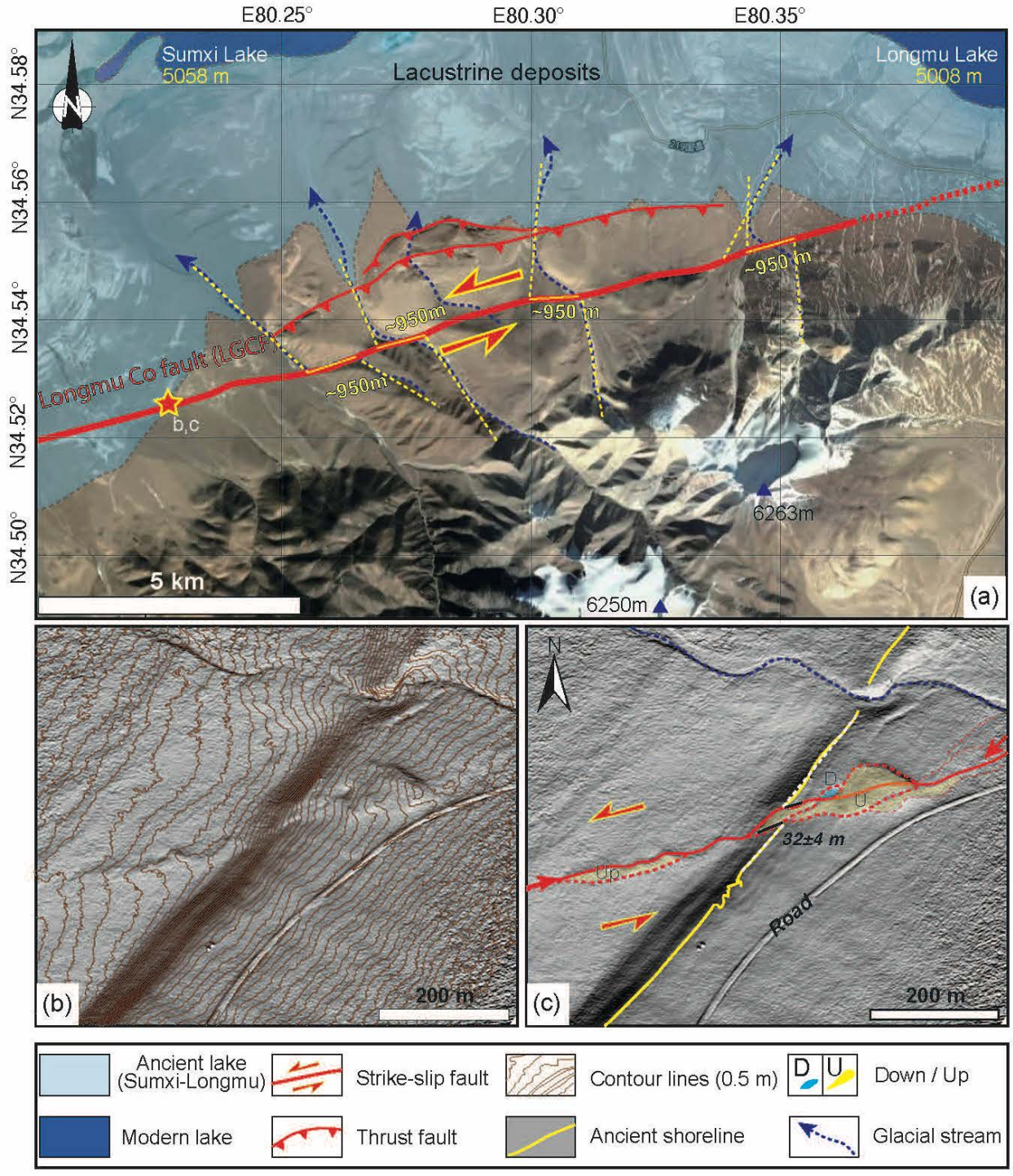

Figure 4. *Late Quaternary offsets along Longmu Co fault south of Sumxi-Longmu Lakes: (a) Active trace of left-lateral fault and associated thrusts. Post-Marine oxygen Isotope Stage MIS-6 glacial valley offsets (950±50 m) and location of offset of highest shoreline of paleo-Sumxi-Longmu Lake are indicated by dashed blue lines and red star, respectively. (b) UAV-derived DEM and (c) cumulative surface breaks and highest shoreline (~6 ka) offset (~32 m), with push-*

200 *ups (Up, yellow shades) and pull-apart (Down, blue shade). Figure location is indicated in*
201 *Figures 1a and 13a. See text for details.*
202

203 ## 3 Morphology, extent and offsets of the Taersa fans/terraces

204 The Taersa site exposes four main alluvial fan and terrace surfaces (from T0, youngest, to
205 T4, oldest), with several smaller, intermediate sub-levels (nine in total, Fig. 3). The broadest
206 levels (T2, T3-T3' and T4) extend far on both sides of the Taersa tributary valley, north of the
207 Karakax river. They correspond to three main generations of large interglacial fill-fans, that
208 spread out broadly as the tributary reached into the main river valley. The curved, convex-
209 upward, shapes of most of the uplifted terraces indicate that they correspond to conical alluvial
210 fan surfaces (e.g., Meyer et al., 1996; Peltzer et al., 2020), which accounts for their slightly
211 different elevations east and west of the tributary valley (Fig. 5b). Most of the other tributary
212 streams have deposited similar imbricated alluvial fan surfaces along the Karakax valley (Li et
213 al., 2012; Peltzer et al., 2020). The lowest/youngest terraces (T0, T0', and T0''), not far from the
214 current river-bed, are covered with small boulders (<1 m in diameter, Figs. 8f,g and S5)
215 deposited along recent, well-preserved braided channels (Fig. 3d). They are separated by small
216 risers, 1-2 m-high at most (Figs. 3e and 5e). North of the fault, one additional young (low)
217 terrace (T1) has been narrowly preserved (Fig. 3c,e), which we interpret to attest to the oblique
218 component of footwall uplift north of the fault (Fig. 5a,c). Such uplift also promoted stronger
219 lateral erosion of the upstream risers, hence affected their geometries more than that of their
220 shielded counterparts south of the fault and east of the tributary (e.g., Cowgill, 2007; Gold et al.,
221 2009; Mériaux et al., 2012).

222 The much smoother, higher fan surfaces T2-T4 are covered with fewer cobbles (Fig. 8b-e).
223 South of the fault, their risers are higher than those of the T0s-T1 flight, from 5 to 25 m, up to a

maximum of 56 m above the present-day river-bed (Figs. 3c,e, insets and 5). North of the fault, that maximum height reaches ~70 m (Fig. 5b). This shows that here, the Karakax main sinistral strand has a significant normal slip component, which we interpret to reflect extension along the northern edge of a pull-apart sag beneath the swampy meanders of the Karakax river east and west of Taersa (Fig. 2). Note that this pull-apart also corresponds to a southwestwards step where the main fault trace crosses the Karakax river from north to south. The pull-apart-related, extensional component has been long-lived since the cumulative vertical throw of fan surfaces T2 to T4 across the fault increases from 2 to 28 m (Fig. 5c). Also, the presence of triangular facets on both the north and south sides of the Karakax valley along mainly that stretch of the KXF supports long-term extension across that pull-apart sag (Figs. 2, S7f and S8f).

On the eastern side of the Taersa tributary floodplain, the T0'/ T0 and T0"/T0' risers, one large fluvial paleo-channel within T0", and the T2/T0" riser (recall that T1 is not present south of the fault) are left-laterally offset by 6±1, 12±1, 18±2, and 24±2 m, respectively (Fig. 3e), as measured in the field with a tape (Li et al., 2012). Note that the offsets of the channel axes and of the tops and bases of their bounding risers are indistinguishable and that, because of exceptional preservation due to the arid climate, the error bars on their offsets are generally on order of 10%. Using Stewart et al. (2018)'s "3D_Fault_Offsets" code, the corresponding, best-fitting horizontal offsets are 5.9±0.5 m for T0/T0' (Fig. S1), 12.8±2.5 m for the T0'/T0" riser (Fig. S2), 17.8±1.5 m for the gully on T0" (Fig. S3), and 22.9±1.5 m for the T0"/T2 riser (Figs. S4, S6 and S7e) while vertical offsets are negligible (<1 m). The automatic restorations thus yield offsets that are consistent (at the 99% level) with our previous field and LiDAR survey measurements. The largest (~23-24 m) offset is also found across several other Holocene fans and fan risers along the Karakax valley (Fig. 1b and Li et al., 2012).

247 The current left-lateral offsets of the higher/older T3/T2, T3'/T3 and T4/T3' riser bases and
248 tops are 200±20, 255±5, and 255±10 m (Figs. 3c and S6) and 196±10, 255±10 and 214±10 m
249 (Fig. 5a), respectively. That the offset of the T4/T3' riser top (~214 m) is significantly smaller
250 than that of the T3'/T3 riser (~255 m), which stands as much as 38 m down below T4 north of
251 the fault (Fig. 5b), and therefore must be much younger, poses problem. This implies that, here,
252 riser tops cannot simply be used to reliably measure cumulative offsets. One way to account for
253 that puzzling observation is that greater incision associated with the vertical uplift north of the
254 fault affected the now preserved apparent horizontal offsets. In addition, the presence of yet
255 another, intermediate, barely preserved terrace ledge (T3'') between T4 and T3' (Figs. 3c, 5-8)
256 implies that the total incision between the T4 and T3' levels was long-lived, and entailed several
257 distinct episodes. Such long-lasting incision events likely broadened the valley width north of the
258 fault at the T4 level by more than 2 x 70 m (possibly as much as 258 m on the east side, Fig. 6a).
259 North of the fault, this laterally eroded the currently narrow, remnant, footwall terrace ledges (T2,
260 T3, T3' and T3''), and particularly the highest uplifted T4 fan riser. On the west side of the
261 Taersa tributary, the more steeply incised valley edge (~30° east dip on average compared to ~18°
262 west dip on average on the east side, Fig. 6a), likely accounts for the complete demise of all
263 surfaces younger than T4, compared to the preservation of the east side ledges.
264 At a more detailed level, Figure 6b shows that the average slopes of the risers on the east
265 side of the Taersa tributary decrease stepwise upwards from ~25° to ~18°, as their overall
266 convexity increases with height, hence age, above river. This is consistent with the much greater
267 degradation of the riser slopes north than south of the fault, which is clear on both the Ikonos
268 imagery (Fig. 6c,d) and in the field (Fig. 8a). The composite T4/T3''/T3' riser, in particular, has
269 been much more strongly incised by deeper and more numerous gullies perpendicular to the

Taersa tributary north than south of the fault (Figs. 6c,d and S7a). That the gullies south of the fault are narrower and shallower than those to the north is supported by the multiple yak/sheep paths that cross them, while none are observed to the north (Fig. 6c,d). Note that similar, asymmetric, fan/terrace aggradation and degradation processes have been described elsewhere along the eastern Altyn Tagh fault (e.g., Pingding Shan, Mériaux et al., 2012). Clearly, the strong erosional degradation of the highest, T4/T3' riser east of the Taersa tributary, and its correlative eastward retreat, make it challenging to use its present geometry to constrain a total cumulative offset in a traditional way.

In order to do so, one must factor in that the top offset must have been greater than apparent today (214 m, Fig. 5a). Before tectonic uplift and correlative river incision and valley widening north of the fault (Fig. 6a), the initial, upstream position of the top of the western riser of T4 east of the tributary (and to a lesser degree, possibly also of those of T3, T3' and T3'') must have been closer to the eastern edge of the Taersa tributary floodplain. A plausible position for the original western edge of T4 east of the tributary might have been between the present T0"/T0' and T1/T0" risers, which mark the current minimum and maximum limits of that floodplain, ~48 m apart (Fig. 3c). This would also be in keeping with the fact that the upstream Taersa tributary valley is deeply anchored, hence captive, within basement rocks that crop out on either side of the tributary valley almost all the way down to the KXF (Figs. 3a and S7). Consequently, the 214 m apparent riser top offset of T4 might be increased to an average of 496±24 m (Figs. 3c and 7).

The two highest risers north and south of the fault are T4/T3' and T3/T2. The T3'/T3 riser, which is only ~3 to 5 m-high, compared to ~25 m for T4/T3' and ~12 m for T3/T2 (Fig. 5b), appears to be an intermediate feature, likely linked with a minor aggradation/incision change between the main climatic episodes that have shaped the Taersa tributary valley and alluvial fan

deposition. In addition, south of the fault trace, the T3'/T3 riser may have been degraded by the passage and recent incision of the large, mountain-sourced gullies that cross obliquely westwards most of the fan surfaces all the way to the Karakax river (Figs. S8 and S9). The fact that the T3'/T3 riser offset (indistinguishable top and base, 255±10 m) is the same as that of the base of the T4/T3' riser, while their ages ought to be different, also poses problem. However, bearing in mind that T4/T3' and T3/T2 reflect the two major fan depositional events, coeval with the strongest glacial-interglacial transitions, the T3'/T3 offset value should nevertheless be taken into account.

The largest possible offset of the T4/T3' riser top (496±24 m) is comparable to that of the southeasternmost T4 fan outer limit along the Karakax river (~500±50 m, Fig. 7a,b). That latter offset, as reconstructed in Figure 7a, also realigns the T4/T3' riser top south of the fault with the current eastern limit of the Taersa floodplain north of the fault (equivalent to the T0"/T0' riser), which independently validates the inference made regarding the initial position of that riser. As shown in Figure 7c,d, it is also possible to use 10 m-resolution, Tandem-X DEM data to assess in section the reconstruction of the initial T4 fan geometry. The best reconstructed fan shape corresponds to horizontal and vertical back-slip displacements of ~500±50 m and ~40±10 m, respectively. Such a ~500±50 m horizontal back-slip is the largest to still preserve a ~130 m-wide passage for the Taersa tributary channel, broad-enough for it to flow between the T4W upstream and T4E downstream risers at the time (206±25 ka). This corroborates the inference that, on both its west- and southeast-facing limits, the original geometry of the T4 fan since abandonment has accrued approximately 500 m of sinistral offset along the KXF.

Lastly, it should be noted that the offset of the T3'/T3 riser at Taersa (~255 ±10 m) is commensurate with that of the corresponding Eemian T4 fan reconstruction (300±20 m) at Site 4 in Peltzer et al. (2020) located 18 km to the east (Fig. 1b).

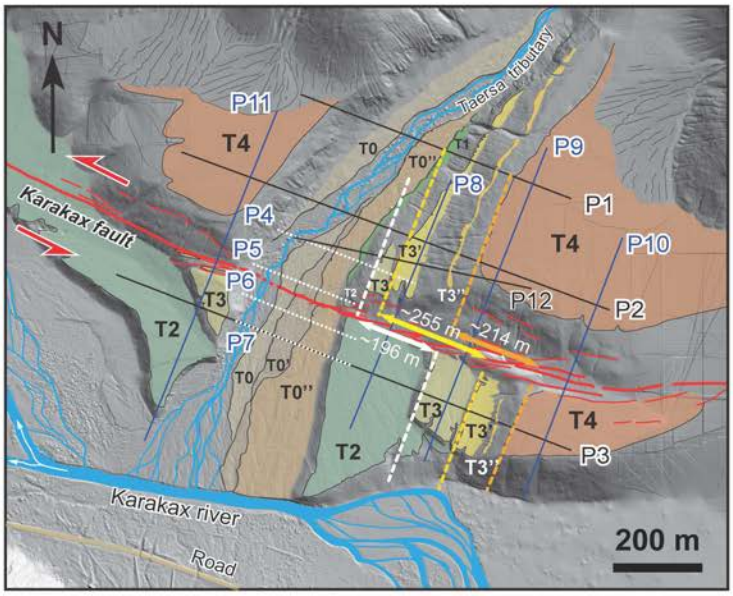
N
P11
T4
T0
T0''
T1
Taersa tributary
P9
P8
P1
Karakax fault
P4
P5
T3'
T4
P10
P6
T3
T2
T3'
T3''
P12
P2
~255 m
~214 m
P7
~196 m
T0
T0'
T0''
T3
T3'
T4
T2
P3
T3''
Karakax river
Road
200 m

(a)

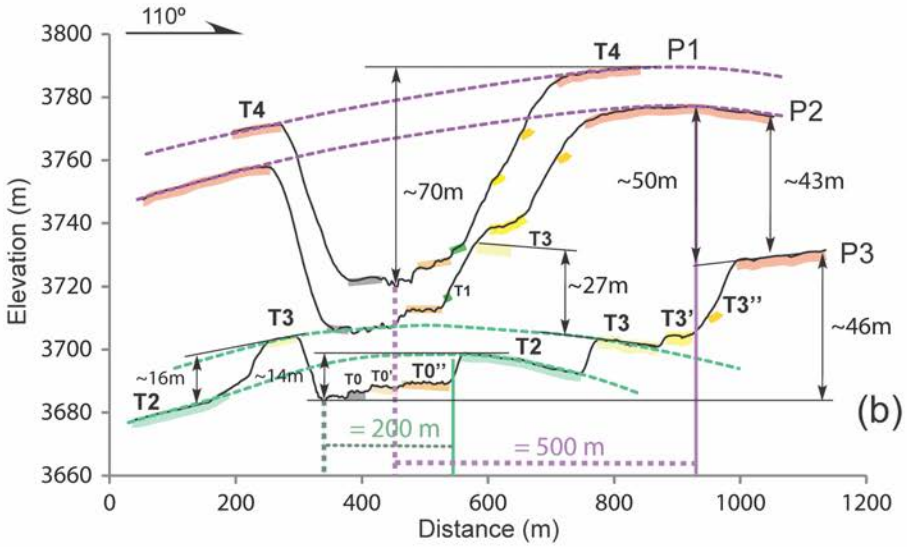
110°
3800
3780
3760
3740
3720
3700
3680
3660
Elevation (m)
T4
P1
T4
P2
~70m
~50m
~43m
T3
P3
~27m
T1
T3
T3
T3'
T3''
~46m
T2
~16m
~14m
T0
T0'
T0''
T2
= 200 m
= 500 m
0
200
400
600
800
1000
1200
Distance (m)

(b)

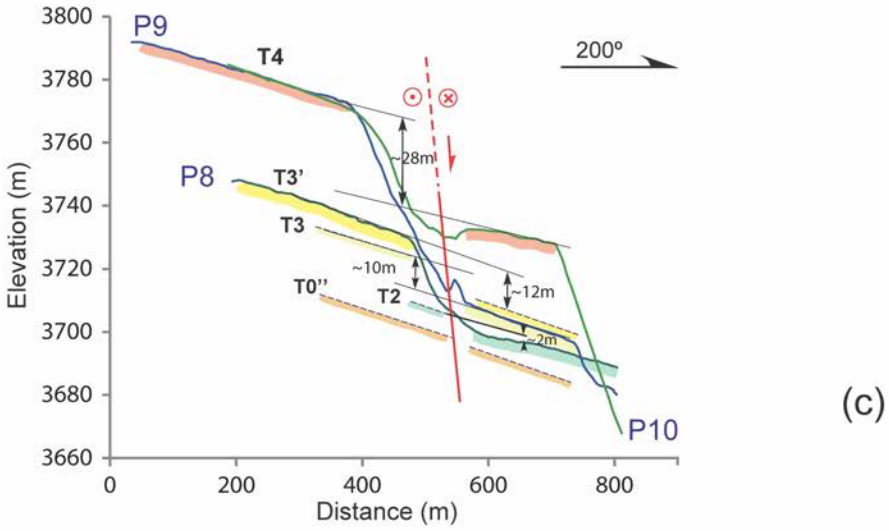
3800
3780
3760
3740
3720
3700
3680
3660
Elevation (m)
P9
T4
200°
~28m
P8
T3'
T3
~10m
~12m
T0''
T2
~2m
P10
0
200
400
600
800
Distance (m)

(c)

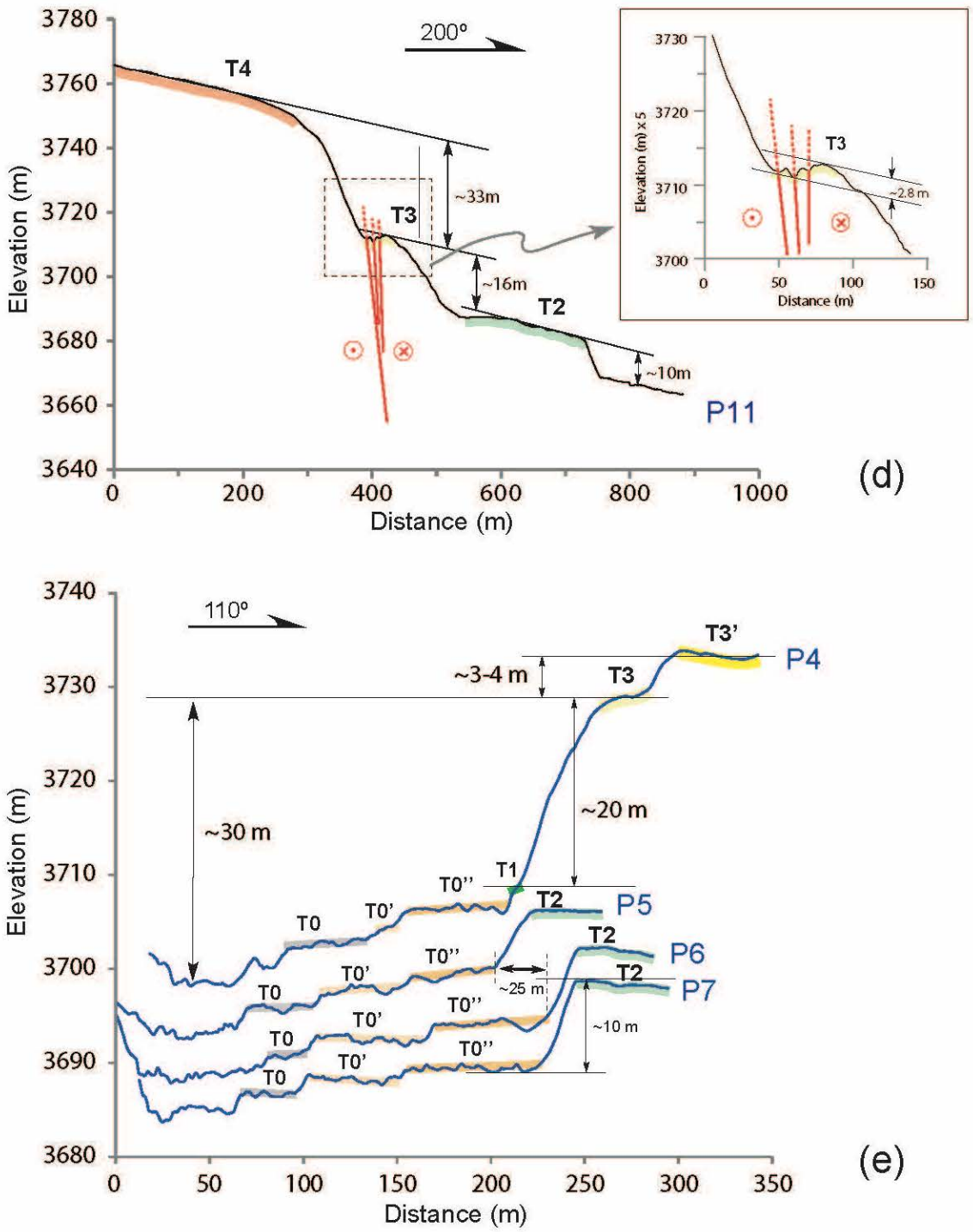

Figure 5. *(a) Annotated LiDAR DEM of Taersa fan and terrace surfaces with location of LiDAR-survey topographic profiles parallel (b and e) and perpendicular (c and d) to the Karakax fault (vertical exaggeration x5). Note convex-upwards shape of profiles parallel to fault (purple and green dashed lines), demonstrating fluvial fan origin of surfaces. Numbers indicate*

relative heights and distances between fan top (apex) and river bed (200 and 500 m), up- and downstream from the fault, respectively. Maximum cumulative co-seismic offset on T0" (~25 m) is also indicated in (e). Note the uplifted, remnant shutter ridges (likely derived from the displacement of T4) in c (P9) and d (P11). Profile P12 is shown in Figure 6b.

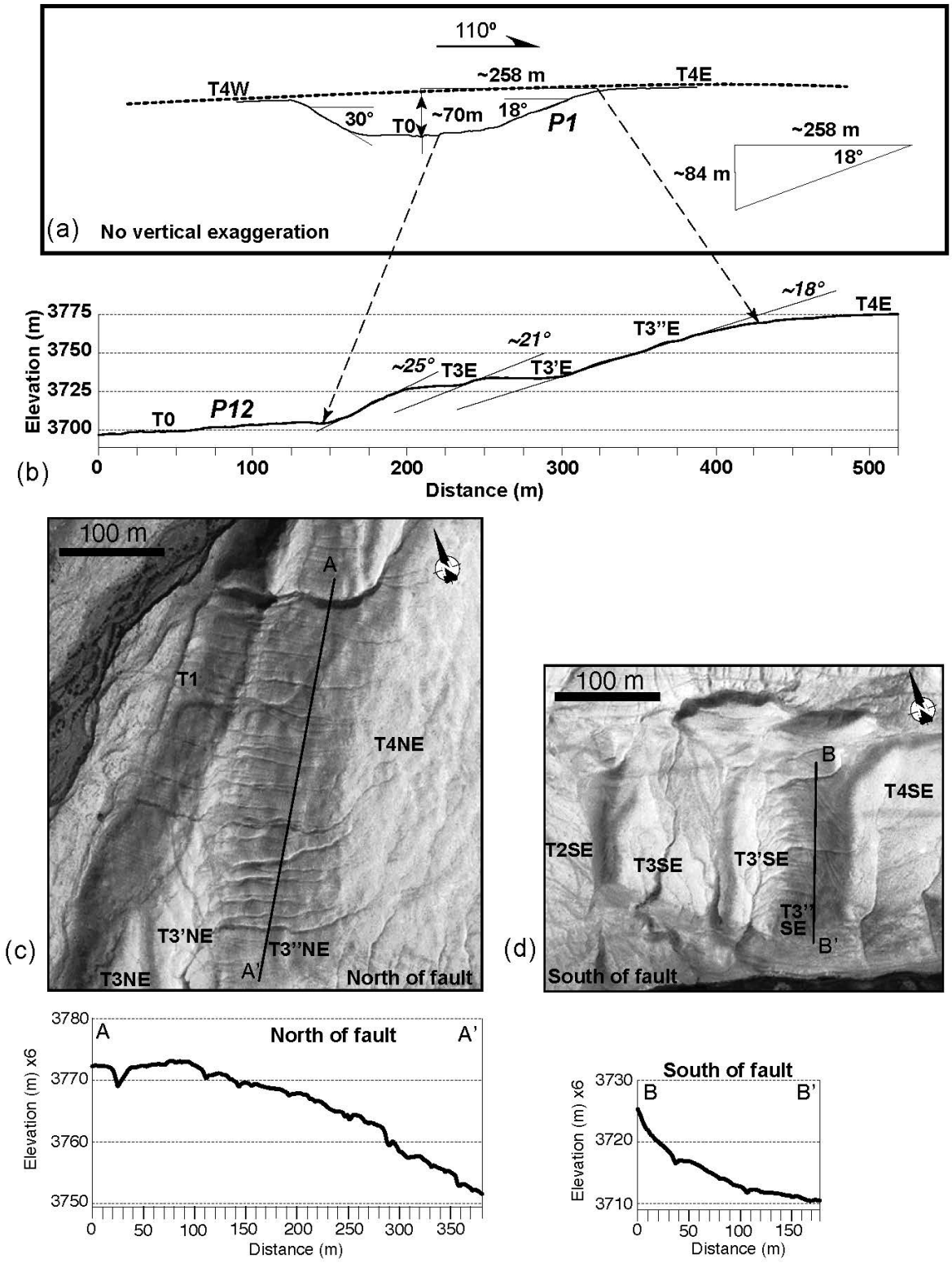

329

330 ***Figure 6.*** *Morphology of the Taersa risers: (a) Profile P1 (see location in Fig. 5a) showing*

331 *comparable elevations of T4E and T4W north of fault with incision depth of Taersa tributary,*

and average upstream valley slopes. (b) Higher resolution profile (P12 in Fig. 5a) showing step-wise steepening (18 to 25°) of average riser slopes (T4/T3', T3'/T3, T3/T1) as a function of younger age. (c and d) Close-up of Ikonos image (see location in Fig. 7a) showing varying degrees of rill incision on west-facing risers north and south of fault, respectively.

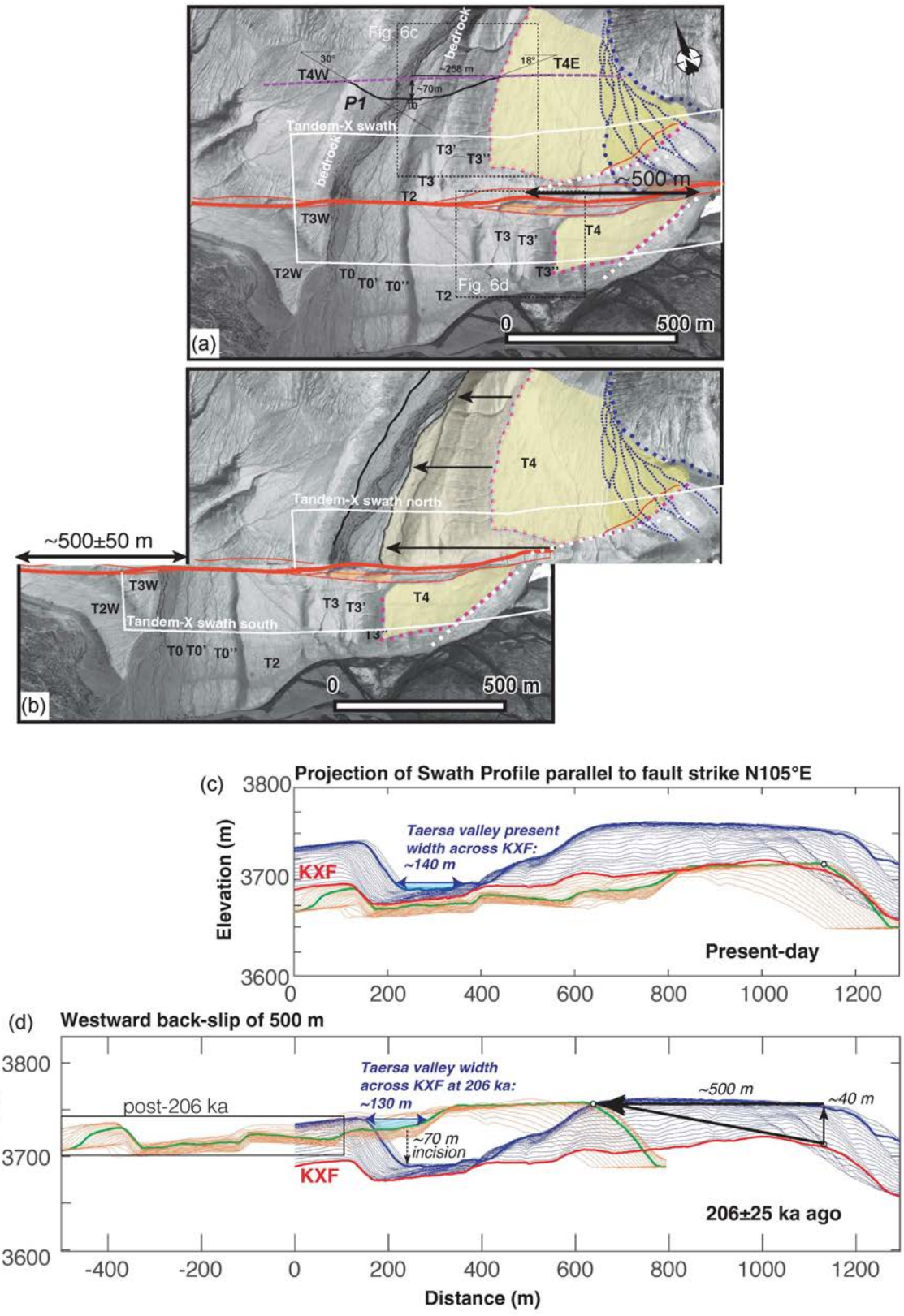
Fig. 6c
bedrock
30°
T4W
~258 m
18°
T4E
P1
~70m
10°
Tandem-X swath
T3'
T3''
T3
T2
~500 m
T3W
T3 T3'
T4
T2W
T0 T0' T0''
T2
Fig. 6d
0
500 m
(a)
T4
Tandem-X swath north
~500±50 m
T3W
T2W
Tandem-X swath south
T3 T3'
T4
T3''
T0 T0' T0''
T2
0
500 m
(b)
(c)
Projection of Swath Profile parallel to fault strike N105°E
Elevation (m)
3800
3700
3600
Taersa valley present width across KXF: ~140 m
KXF
Present-day
0
200
400
600
800
1000
1200
(d)
Westward back-slip of 500 m
Taersa valley width across KXF at 206 ka: ~130 m
~500 m
~40 m
post-206 ka
~70 m incision
KXF
206±25 ka ago
-400
-200
Distance (m)

Figure 7. *Reconstruction of the complete sinistral offset of oldest T4 fan surface taking into account normal component of uplift along left-lateral Karakax fault at Taersa site: (a) Ikonos image-based interpretation of T4 fan surface (pale yellow) including younger drainages to the east (on darker yellow fan). Position of profile in Figure 6a is indicated across upstream Taersa valley. East-west elongated, orange hills along main KXF trace (red) are shutter ridges likely derived from T4 (see also profiles in Fig. 5c,d). (b) Reconstruction of complete shape of T4 fan before uplift of T4north and incision of Taersa tributary north of fault, consistent with a ~500±50 m total offset of both western and southeastern edges of fan. See text for details. (c) Projection, along KXF at Taersa, of 400 m-wide topographic profiles swath (20 south of fault, red; 20 north of fault, blue) from Tandem-X DEM (vertical exaggeration x2). Red line is KXF fault trace. Thick dark blue line is present envelope of highest surface (T4) across Taersa valley (light blue shade) north of fault. Thick green line is present envelope of highest surfaces (T4-T3'-T3) across Taersa valley south of fault. (d) Reconstruction of ~500 m westward back-slip (as in b) of red profiles south of fault (vertical exaggeration x2). Note preservation of ~130 m-wide valley width across fault at ~206 ka, similar to present valley width (~140 m). Black vectors to the right indicate vertical and left-lateral offsets across KXF since 206 ka.*

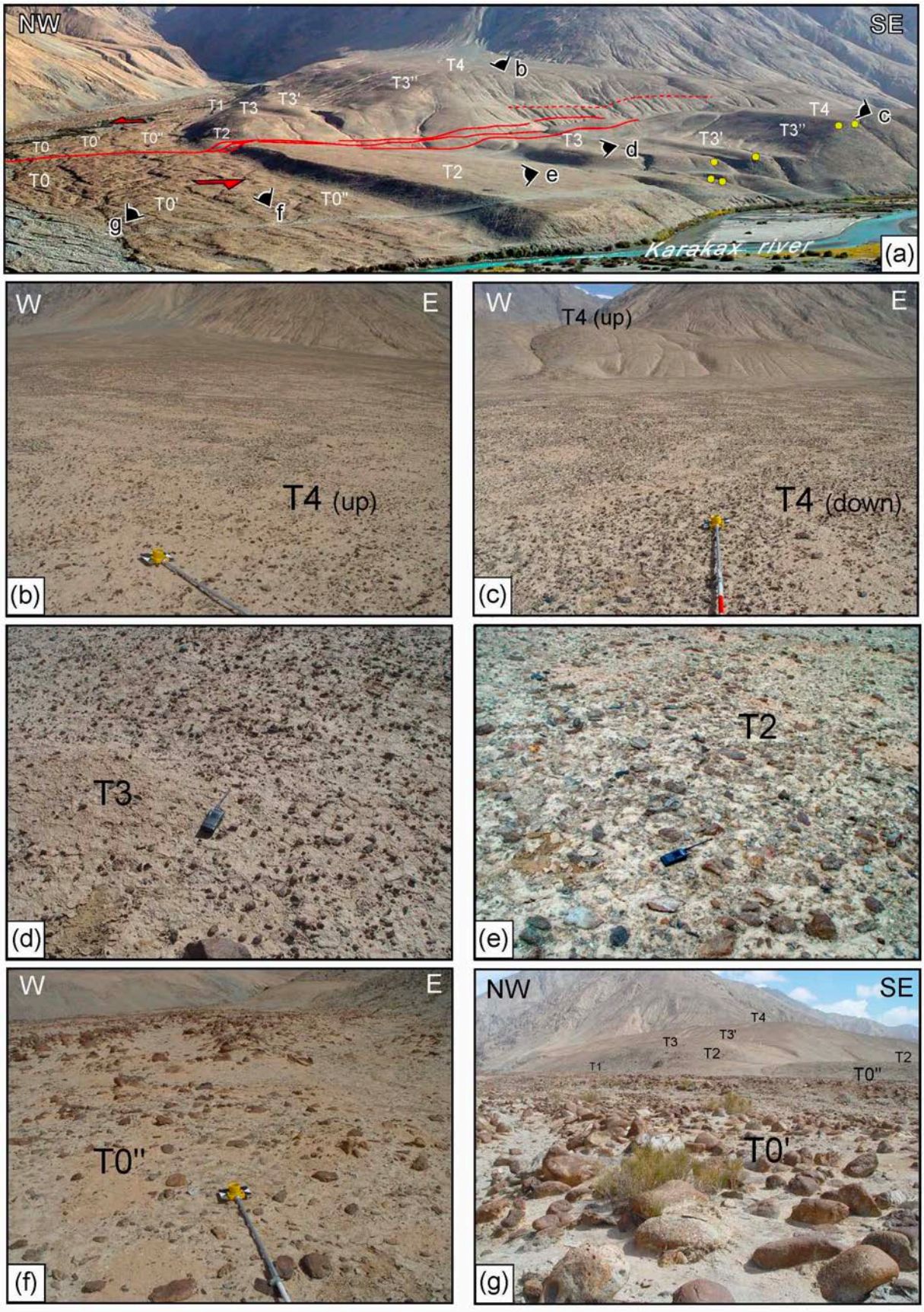
NW
SE
T4
b
T3''
T1
T3
T3'
T4
c
T3''
T0
T0'
T0''
T2
T3
d
T3'
T0
T2
e
T0'
T0''
g
f
Karakax river
(a)
W
E
T4 (up)
(b)
W
E
T4 (up)
T4 (down)
(c)
T3
(d)
T2
(e)
W
E
T0''
(f)
NW
SE
T4
T3
T3'
T2
T1
T2
T0''
T0'
(g)

354

Figure 8. *Field photographs of Taersa fan and terrace surfaces (a) showing distinct cobble sizes and surface roughness as a function of abandonment age north (b) and south (c-g) of the fault. The younger the surface the larger and coarser the samples, as expected. Yellow circles indicate locations of Optically Stimulated Luminescence (OSL) samples from Gong et al. (2017). See text for discussion.*

4 ^{10}Be, ^{26}Al cosmogenic surface and depth profile dating of the alluvial surfaces

The ages of the 35 samples dated on the alluvial surfaces along either sides of the fault and Taersa tributary valley (Fig. 3c) are shown in Table 1 and plotted in Figure 9.

The youngest ^{26}Al age on T4 may be statistically rejected as a clear outlier, using Chauvenet criterion, while the 13 remaining ages (12 ^{10}Be and one ^{26}Al on both T4E and T4W) range between 162 and 245 ka, with an average of 206±25 ka (1 σ). This confirms that the highest T4 surfaces belong to the same large fan on both sides of the Taersa tributary. Note that the T4 alluvial surface dated at Taersa (the oldest age is 245±16 ka) is amongst the oldest ever dated in and along the margins of Tibet (e.g., Hetzel et al., 2002; Blisniuk and Sharp, 2003; Tao et al., 2020). This attests that regional erosion of the surface tops is minimal, as previously suggested in other areas of NE Tibet (e.g., Hetzel et al., 2002).

The two sample ages on T3' (191 and 215 ka) yield an average age of 203±18 ka, comparable to that of T4. The narrow widths of T3', at the base of the high T4/T3' risers that bound the west sloping surfaces of T4 (Fig. 3c), suggest that both samples might have foundered from T4, likely due to co-seismic shaking. High-resolution satellite images and broad-scale field photograph (Fig. 8a) confirm that much of the T4/T3' riser slope is covered with large boulders that have toppled down during rockfalls. This likely accounts for their apparently similar ages, despite the large elevation difference (~43-50 m north, and ~25 m south of the fault, Fig. 5b).

The age distribution on T3 is completely different east and west of the Taersa tributary (Fig. 9). To the east, the concordant average ages of the three samples is 185±2 ka, a value roughly consistent with the average ages on T3' and T4. We thus infer that they were similarly transported out of T4, likely along the large south-flowing gullies that drain it (Figs. S8 and S9). To the west, by contrast, the two samples collected on the surface of the small remnant of T3, which is separated from T4 by a ~2-3 m-deep sag along the fault (Figs. 3 and 5d), have much younger ages (97±6 and 127±8 ka) (Fig. 9). Such ~100 ka-younger ages are consistent with the elevation differences between T4 and T3 (~33 m, Fig. 5d), or T3 and T0 (~26 m, Fig. 5d) on the Taersa tributary west bank. These ages are also similar to those found by Peltzer et al. (2020) on their highest surfaces (T4) ~30 m above the local tributary at their Site 4. Hence, although we have only two in situ ages for now, we infer that the average age (112±21 ka) of our two samples on T3W represents the actual age of the Taersa T3-T3' surfaces. At a more detailed level, one might further hypothesize that the small, ~3-5 m-high riser between T3 and T3' east of the Taersa tributary corresponds to that observed by Peltzer et al. (2020)'s between their T3 and T4 surfaces at their Site 4. In that case, the T3 and T3' fan surfaces at Taersa would be even closer in age (97±6 and 127±8 ka) with those dated farther east (~95.9±2.8 and 112.9±6.5 ka). It is clear, however, that additional sampling would be needed to confirm that inference.

At the level of T3' north of the KXF, one depth profile was retrieved from a refreshed riser in a deep incision that reaches the top of T4 (Figs. 3c and S7). Four individual cobbles collected between 55 and 120 cm-depths yield consistent ^{10}Be and ^{26}Al model ages of ~260 and ~256 ka (Fig. 10). Such ages, however, are ~50 ka older than the average age (~206 ka) of the T4 surface above, which is stratigraphically puzzling. They might be interpreted to date reworked colluvium

derived from the erosion of surfaces higher than T4, upstream along the Taersa tributary. In any case, these old 'inherited' ages must predate the abandonment of either T3' or T4.

On T2, which is well-preserved only south of the fault, ten surface sample ages (seven ^{10}Be and three ^{26}Al) fall between 11 and 30 ka, with an average age of 19±7 ka. Three ages (~28±2 ka on average), are significantly older, by ~10 ka, than the majority of the seven others (average of 16±3 ka). One depth profile in the refreshed eastern T2/T0" riser (Fig. S5) yields model ^{10}Be and ^{26}Al surface ages between 11 and 20 ka (average of 15.5±4.5 ka), after rejection of two clear outliers (Fig. 10). Such concordant ages confirm that T2, which fans out of the Taersa gorge into the Karakax valley, is best interpreted as a fan-shaped fill terrace, resulting from post-glacial melting.

The morphologies of the lowest terraces (T0-T0'-T0"), that stand 10 m below T2 but only 1-2 m above each other and the present-day river bed, are similar, with remarkably well-preserved braided channels (Figs. 3d,e, 5e and S7b). They must therefore be significantly younger than T2 (~16 ka). The unique sample on T0", with ages of 32 ka (^{10}Be) and 29 ka (^{26}Al) (average of 31±2 ka) must thus be an outlier derived from erosion of T2. Likewise, the two ^{10}Be samples on T0' (16 and 24 ka with an average of 20±6 ka) must also be outliers derived from T2. Finally, the six samples on T0 include two ~20 ka and four 10±2 ka ages, consistent with inheritance of the two older cobbles, while the youngest majority reflects T0's actual Holocene age.

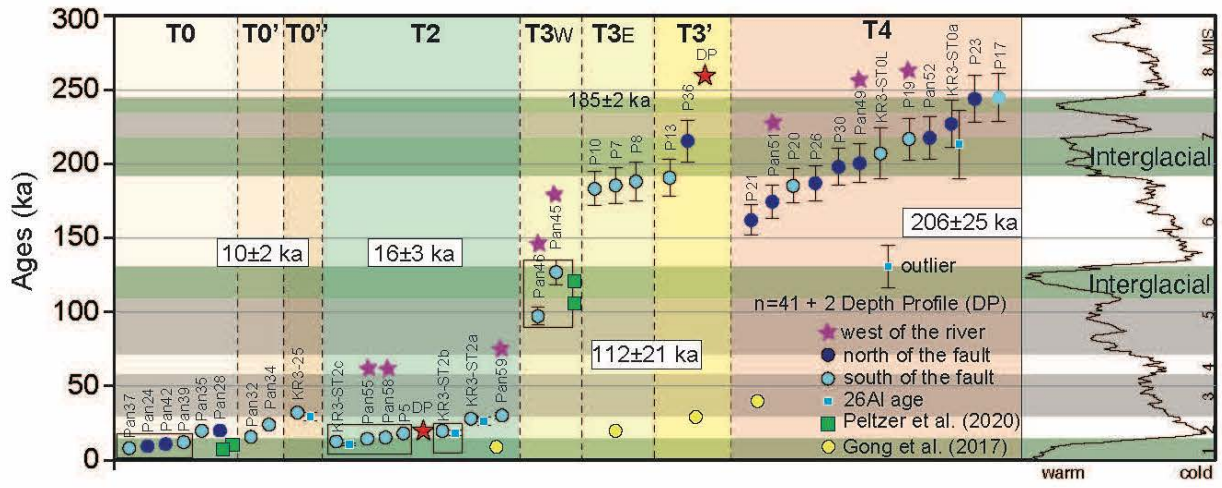

Figure 9. *Ages at the Taersa site.* ^{10}*Be and* ^{26}*Al surface-exposure cosmogenic ages (numbered as in Fig. 3c,e and Table 1) using the Lifton et al. (2014) 'LSDn' model in CRONUS version 3, with 1σ uncertainties. Ages in white boxes are average of all individual ages for T4, and average of ages in thin black boxes for T3W, T2 and T0. Green squares refer to ages from Site 4 in Peltzer et al. (2020) (location in Fig. 1b). Yellow circles are OSL ages from Gong et al. (2017). Right panel shows global climatic proxy curve of Lisiecki and Raymo (2005), with grey-shaded sectors indicating Marine oxygen Isotope Stages (MIS) 1 to 8. Green bands are interglacial periods, during which glaciers melt coeval with deposition of large alluvial fans and terraces. See text for details.*

Table 1: Analytical results of ^{10}Be and ^{26}Al geochronology and surface-exposure model ages at Taersa site along Karakax fault.

Surface	Sample name	Lat (N)	Long (E)	Elev (m)	Depth (cm)	Quartz (g)	Be carrier (mg)	Al carrier (mg)	^{10}Be/^{9}Be (10^{-15})	^{26}Al/^{27}Al (10^{-15})	^{10}Be (10^{6} atom/g)	^{26}Al (10^{6} atom/g)	Lm (+ ext. uncert.)	(int. Uncert.)	LSDn (+ ext. uncert.)	(int. Uncert.)
T0SE	KXW-Pan 39*	36.33562	78.08641	3711	0	20.4503	0.3464	/	450±8	/	0.509±0.009	/	12155±945	237	**12155±758**	237
	KXW-Pan 35*	36.3352	78.0863	3707	0	20.050	0.3461	/	783±10	/	0.903±0.012	/	20261±1555	279	**19751±1204**	272
	KXW-Pan 37*	36.33505	78.0863	3706	0	20.112	0.3465	/	276±7	/	0.318±0.008	/	7908±628	201	**8059±519**	205
T0NE	KXW-Pan 24**	36.33717	78.08839	3729	0	26.138	0.3799	/	379±12	/	0.368±0.012	/	9138±750	299	**9366±633**	307
	KXW-Pan 28**	36.33619	78.08708	3720	0	25.267	0.3774	/	919±26	/	0.917±0.026	/	20414±1651	592	**19881±1314**	577
	KXW-Pan 42**	36.33612	78.08694	3719	0	24.964	0.3796	/	421±14	/	0.428±0.014	/	10524±871	361	**10716±733**	368
T0'SE	KXW-Pan 32*	36.33569	78.08686	3716	0	20.130	0.3464	/	614±8	/	0.706±0.009	/	16066±1232	224	**15737±959**	219

	KXW-Pan 34*	36.33534	78.08664	3710	0	20.101	0.3455	/	991±14	/	1.138±0.016	/	24867±1914	355	**23934±1464**	342
T0"SE	KR3-25 $	36.33441	78.08694	3710	0	15.008	0.4259	/	921±17	/	1.79±0.049	/	33792±2731	941	**32046±2109**	892
								2.2233	/	2815±106	/	9.639±0.372	*26Al: 29973±3099*	*1177*	***26Al: 29475±2826***	*1157*
T2SE	KXW-P5**	36.3336	78.0889	3714	0	25.657	0.3801	/	824±19	/	0.816±0.019	/	18407±1457	440	**17994±1151**	430
	KR3-ST2-a $	36.33433	78.08817	3710	0	15.848	0.4395	/	841±16	/	1.56±0.044	/	29182±2359	824	**27902±1839**	787
								2.1199	/	2745±89	/	8.518±0.359	*26Al: 26577±2780*	*1137*	***26Al: 26195±2547***	*1121*
	KR3-ST2-b $	36.33433	78.08817	3710	0	15.183	0.4376	/	540±11	/	1.041±0.029	/	20158±1625	569	**19655±1292**	555
								7.7873		473±25	/	5.635±0.299	*26Al: 18274±1993*	*979*	***26Al: 18406±1879***	*986*
	KR3-ST2-c $	36.33433	78.08817	3710	0	15.154	0.4361	/	320±6	/	0.616±0.018	/	12618±1016	360	**12583±827**	359
								2.5932	/	716±33	/	2.841±0.148	*26Al: 10096±1091*	*529*	***26Al:10588±1071***	*555*
DP T2	KR3-3 $	36.33433	78.08817	3710	50	15.006	0.4364	2.6239	1027±20	2614±95	1.998±0.056	10.613±0.522	/	/	/	/
	KR3-12 $	36.33433	79.08817	3710	106	15.126	0.6625	1.1776	312±11	2565±112	0.916±0.037	4.646±0.231	/	/	/	/
	KR3-13 $	36.33433	80.08817	3710	110	15.106	0.6573	2.4222	87±4	372±24	0.254±0.013	1.388±0.119	/	/	/	/
	KR3-18 $	36.33433	81.08817	3710	130	15.389	0.6546	2.0230	53±2	286±31	0.15±0.007	0.874±0.103	/	/	/	/
	KR3-20 $	36.33433	82.08817	3710	140	13.499	0.4570	0.9900	92±3	714±41	0.208±0.008	1.217±0.072	/	/	/	/
T2SW	KXW-Pan 55**	36.33561	78.08362	3705	0	25.572	0.3786	/	640±20	/	0.633±0.02	/	14634±1202	477	**14405±975**	470
	KXW-Pan 58**	36.33506	78.08346	3699	0	27.118	0.3784	/	726±23	/	0.677±0.021	/	15577±1279	506	**15292±1034**	497
	KXW-Pan 59**	36.33455	78.08461	3703	0	25.830	0.3783	/	1493±47	/	1.461±0.046	/	31770±2615	1019	**30135±2039**	966
T3SE	KXW-P8**	36.33362	78.09042	3717	0	6.862	0.3734	/	2535±75	/	9.221±0.275	/	199175±17190	6351	**188071±13245**	5975
T3SE	KXW-P7**	36.33354	78.09035	3716	0	20.886	0.2935	/	9683±176	/	9.118±0.166	/	195720±16139	3812	**185330±12184**	3597
T3SE	KXW-P10*	36.33332	78.09059	3714	0	20.008	0.3277	/	8148±54	/	8.917±0.059	/	193279±15530	1376	**183143±11565**	1300
T3SW	KXW-Pan 46*	36.33608	78.08486	3724	0	20.106	0.3461	/	4079±23	/	4.692±0.026	/	101486±7897	596	**97092±5945**	570
T3SW	KXW-Pan 45**	36.33597	78.08498	3721	0	16.5205	0.3794	/	4126±96	/	6.331±0.1476	/	135174±11109	3298	**126805±8394**	3085
T3'SE	KXW-P13**	36.33289	78.09108	3711	0	22.405	0.3793	/	8259±111	/	9.343±0.125	/	202703±16535	2920	**190625±12299**	2735
T3'NE	KXW-P36**	36.33745	78.09018	3758	0	25.269	0.3797	/	10861±141	/	10.905±0.142	/	232977±19185	3293	**215461±14000**	3028
DP T3'	KR3-29 $	36.33921	78.09165	3770	55	12.7368	0.3639	2.1456	4331±58	10441±361	8.279±0.199	40.878±2.006	/	/	/	/
	KR3-31 $	36.33921	79.09165	3770	100	35.0026	0.4584	1.7434	5883±84	25547±771	5.155±0.127	29.537±0.905	/	/	/	/
	KR3-33 $	36.33921	80.09165	3770	110	20.8226	0.3026	2.0375	3820±74	8206±235	3.715±0.103	18.688±1.001	/	/	/	/
	KR3-34	36.33921	81.09165	3770	120	24.5691	0.2943	5.9325	4910	3497±	3.935±0.129	19.33	/	/	/	/

	$								±128	112		5±0.6 27					
T4SE	KXW-P20*	36.33283	78.09419	3740	0	20.372	0.3272	/	8540 ±59	/	9.165±0.063	/	195637±15738	1455	**185071±11701**	1371
	KXW-P17**	36.33317	78.09257	3733	0	25.926	0.3796	/	1231 4±16 5	/	12.046±0.161	/	263775±21969	3870	**244714±16081**	3567
	KXW-P19**	36.33271	78.09392	3736	0	25.267	0.3794	/	1078 3±14 5	/	10.82±0.145	/	234059±19299	3411	**216647±14103**	3139
	KR3-ST0L *$*	see map	see map	3740	0	15.110	0.4376	/	6192 ±281	/	11.998±0.596	/	222489±21572	11912	**206956±17113**	11022
								2.3834	/	11867 ±519	/	43.57 2±2.3 76	*26Al: 135936±15988*	*8022*	***Al26: 130901±14384***	*7702*
T4NE	KR3-ST0a *$*	see map	see map	3790	0	15.001	0.4363	/	6927 ±132	/	13.482±0.373	/	245894±21358	7397	**226885±15962**	6781
								2.3458	/	19579 ±511	/	71.05 2±2.9 34	*26Al: 223583±26172*	*10525*	***26Al: 213150±23039***	*9972*
	KXW-P30*	36.3356	78.09543	3786	0	20.265	0.3288	/	9412 ±65	/	10.206±0.07	/	213090±17244	1591	**197897±12566**	1470
	KXW-P21**	36.3347	78.09499	3771	0	24.5581	0.379	/	7936 ±108	/	8.185±0.1112	/	173423±14011	2497	**161960±10354**	2323
	KXW-P23**	36.33473	78.09479	3771	0	24.965	0.3797	/	1208 0±15 7	/	12.276±0.159	/	263360±21912	3751	**243802±15993**	3449
	KXW-P26**	36.33454	78.09664	3748	0	26.150	0.3791	/	9626 ±127	/	9.326±0.123	/	198063±16122	2794	**186999±12039**	2628
T4NW	KXW-Pan 52**	36.33884	78.08673	3776	0	26.497	0.3796	/	1161 6±20 8	/	11.119±0.199	/	235556±19665	4571	**217467±14428**	4194
	KXW-Pan 49**	36.33823	78.08601	3769	0	17.922	0.2912	/	9467 ±153	/	10.299±0.166	/	215554±17790	3754	**200287±13112**	3470
	KXW-Pan 51**	36.33906	78.08698	3778	0	18.749	0.2906	/	8528 ±140	/	8.856±0.145	/	185259±15142	3242	**174411±11330**	3041

Samples "*" and "**" were collected in 2011 and processed at Stanford University's cosmogenic facility and samples "*$*" were collected in 1995 and processed and measured at Center for Accelerator Mass Spectrometer (CAMS) at Lawrence Livermore National Laboratory (LLNL).

$^{10}Be/^{9}Be$ ratios "*" were measured at CAMS at LLNL and $^{10}Be/^{9}Be$ ratios "**" measured at ASTER (CEREGE).

Ages calculated with the CRONUS 3 calculator (Balco et al., 2008). Lm= Lal (1991)/Stone (2000) time-dependent production rate model. LSDn = Lifton et al. (2014) model ages discussed in text.

"See map" refers to Figure 3c, because no exact GPS location was measured in the field.

Shielding factor is 0.98; Sample density is 2.65 g/cm3 (all samples are quartzite). Thickness was taken as 5 cm.

Standard used at CAMS for samples "*" is 07KNSTD with ^{10}Be isotope ratios = 2.85x10-12. For samples "*$*" standard is LLNL3000 with 10Be isotope rations = 3x10-12. KNSTD is the standard for Al samples.

Standard used at ASTER is NIST SRM4325 (=NIST_27900) with ^{10}Be isotope ratios = 2.79x10-11, equivalent to 07KNSTD.

ext. (int.) Uncert. = external (internal) uncertainty

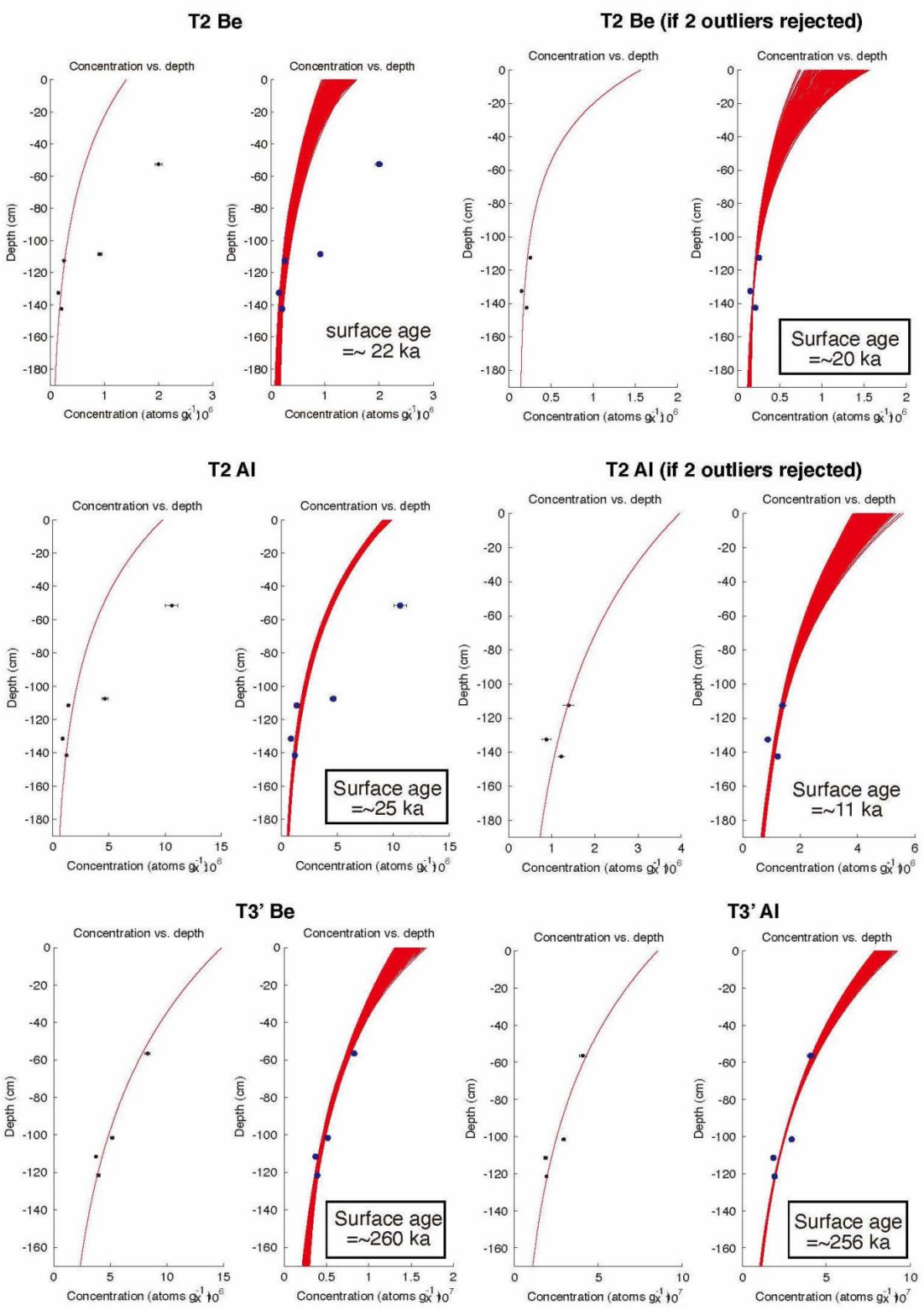

Figure 10. *Depth profile (photos in Figs. S5 and S7) results using the Hidy et al. (2010) software. Model surface ages consistent with* ^{10}*Be and* ^{26}*Al concentrations for T2 and T3' depth profile samples, with or without outliers, are indicated.*

439

440 # 5 Interpretation and discussion

441 ## 5.1 Correlation of terrace ages with climate

442 Whether a stream can transport sediments (hence emplace fans) or incise along its channel
443 (hence abandon terraces) is highly dependent on climate (e.g., Whipple and Tucker, 1999;
444 Mériaux et al., 2012). Typically, during glacial periods, stream power and sediment load are
445 limited, thus unfavorable to fan deposition. Glacier melting at the beginning of interglacials, due
446 to warmer climate, causes rapid increase of stream power and sediment transport, which in turn
447 promotes fill terrace aggradation and broad fan deposition. Conversely, it is well-established that
448 at the end of the warm and humid early Holocene Climatic Optimum (HCO, ~10 to ~5 ka),
449 coeval with lake high-stands on the Tibetan plateau (Gasse et al., 1991), a shift to drier climate
450 led to generally renewed river incision, terrace abandonment and lake level drop throughout
451 North-Africa, Eurasia and Tibet (e.g., Gasse et al., 1990; Avouac et al., 1996; Brown et al., 2003;
452 Li et al., 2005; Van Der Woerd et al., 2002).

453 The four main surface age groups we obtain, 206±25 ka for T4, 112±21 ka for T3-T3' (or
454 ~96 ka for T3 and ~113 ka for T3'), 16±3 ka for T2 and 10±2 ka for T0s, correlate well with the
455 last four warm climatic periods at ~200 ka (MIS-7 interglacial), ~115 ka (Eemian interglacial),
456 ~16 ka (post-Last Glacial Maximum, MIS-2, melting), and ~10 ka (Holocene interglacial) (green
457 bands in Fig. 9). The Eemian and Holocene ages we obtain at Taersa are similar, within
458 uncertainty, to the ^{10}Be ages (~110 and 11 ka) found 18 km to the east, north of the Karakax
459 river by Peltzer et al. (2020) (their Site 4: large fan offsets first identified by Peltzer et al., 1989).
460 Likewise, within uncertainty, our youngest terrace ages are consistent with the OSL

abandonment age (~9±1 ka) they found ~10 km west of Taersa (Fig. 1b) for one offset terrace (~10 m above present fluvial channel, their Site 1) of a southern tributary of the Karakax river.

The Taersa site, however, uniquely preserves the oldest (~210 ka) and highest (>110 m above the Karakax river) conical fan surface dated thus far along the Karakax valley, and possibly for now within the northern Tibet Plateau. Consequently, it is possibly also the only site where the largest horizontal and vertical cumulative offsets are preserved along the KXF.

5.2 Fault slip rates since ~210 ka

Combining alluvial surface abandonment ages and riser offsets provides bounds on slip rates over a ~210 ka-long timescale. Matching the T4 abandonment age (206±25 ka) with the total offsets of the current T4 southeastern limit and the inferred western T4 riser top (~500±50 and 496±24 m, respectively) yields 2.4(+0.4/-0.3) mm/yr (Figs. 3c, 7, 11a and Table 2). Combining the T4/T3' current riser base offset (255±10 m) with the inferred oldest age of T3'east (127±8 ka based on that on T3west) yields a minimum rate of 2.0(+0.2/-0.1) mm/yr. Taking the inferred youngest age of T3east (97±6 ka based on that on T3west) with the current offset (255±5 m) of the T3'/T3 riser base yields 2.6±0.2 mm/yr. Matching the offset of the current T3/T2 western riser base (200±20 m) with the inferred youngest 97±6 ka age of T3 yields 2.1(+0.3/-0.2) mm/yr (Figs. 3c, 11a, S6 and Table 2). Lastly, we take the age of the 22.9±1.5 m offset of the base of the T2/T0" riser (Figs. 3e, S4 and S6), that necessarily postdates the total incision (10 m) of T2 (abandoned after 16±3 ka) by the Holocene Taersa tributary, to be 10±2 ka, which is consistent with a slip rate of 2.3(+0.6/-0.4) mm/yr (Figs. 11a,b, S6 and Table 2). The normal throw component across the fault at Taersa may also be estimated using the vertical offsets of T4 and T3' (Fig. 5c). The ~28 m offset of T4 implies a throw rate of 0.14±0.2 mm/yr, while the 12 and

484 10 m vertical offsets of T3' and T3, respectively, are consistent with a throw rate of 0.1±0.01

485 mm/yr.

486

487 **Table 2**. Summary of offsets, ages and slip rates at Taersa.

	Offsets (m)	Ages (ka)	Slip rate (mm/yr)
T4 southeastern limit	500±50	206±25	2.4(+0.4/-0.3)
Original T4 riser at incision onset	496±24	206±25	2.4(+0.4/-0.3)
T4/T3' current base	255±10	127±8	2.0(+0.2/-0.1)
T3'/T3 current base	255±5	97±6	2.6±0.2
T3/T2 current base	200±20	97±6	2.1(+0.3/0.2)
T2/T0" current base	22.9±1.5	10±2	2.3(+0.6/-0.4)
T0"/T0'	17.8±1.5	<10±2	2-3
T0'/T0	12.8±2.5	<10±2	2-3
T0/river bed	5.9±0.5	1882 AD	n/a

488

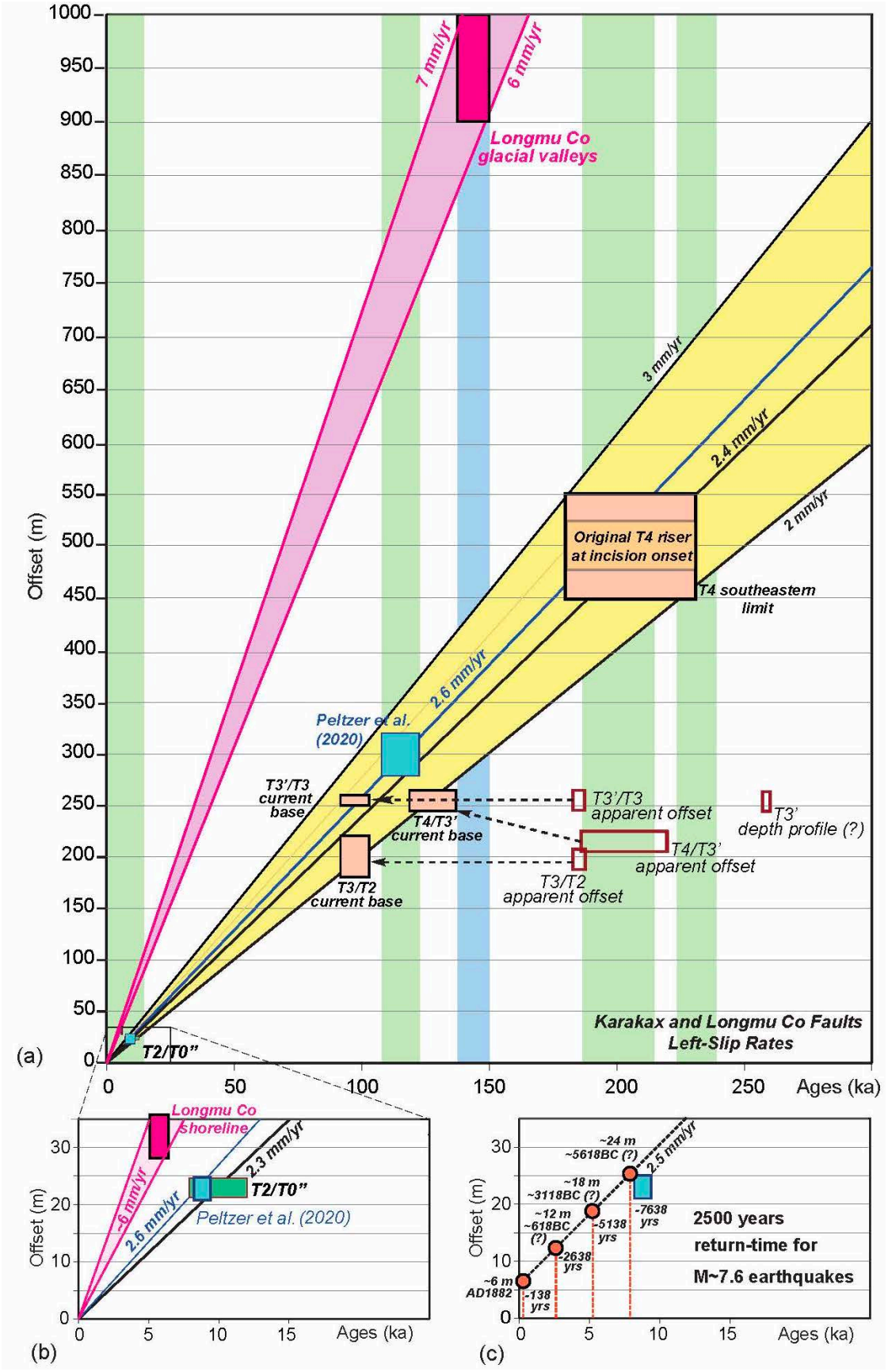
Offset (m)
Ages (ka)
7 mm/yr
6 mm/yr
Longmu Co
glacial valleys
3 mm/yr
2.4 mm/yr
2 mm/yr
Original T4 riser
at incision onset
T4 southeastern
limit
2.6 mm/yr
Peltzer et al.
(2020)
T3'/T3
current
base
T4/T3'
current base
T3/T2
current base
T3'/T3
apparent offset
T4/T3'
apparent offset
T3/T2
apparent offset
T3'
depth profile (?)
Karakax and Longmu Co Faults
Left-Slip Rates
T2/T0"
(a)
Longmu Co
shoreline
2.3 mm/yr
6 mm/yr
2.6 mm/yr
T2/T0"
Peltzer et al. (2020)
(b)
~24 m
~5618BC (?)
2.5 mm/yr
~18 m
~3118BC (?)
~12 m
~618BC
(?)
~6 m
AD1882
-7638
yrs
-5138
yrs
-2638
yrs
-138
yrs
2500 years
return-time for
M~7.6 earthquakes
(c)

489

490 ***Figure 11.*** *Slip rates on Karakax and Longmu Co faults. (a) Late Quaternary slip rates derived*
491 *from offset/age relationships. Dashed black arrows indicate most plausible shifts of offset and*
492 *ages of risers east of Taersa tributary based on T3 ages west of tributary (see text for details).*
493 *Green bands are interglacial periods as in Figure 9, blue band is coldest glacial within MIS-6.*
494 *See text for details. (b) Zoom on youngest terrace age range, including Peltzer et al. (2020)*
495 *result. (c) Inferred large earthquakes return times consistent with simplified characteristic co-*
496 *seismic slip (~6 m) and constant Holocene ~2.5 mm/yr slip rate.*
497

498 Overall, the above left-lateral rates (Table 2) range between extreme values of 1.9 and 2.9
499 mm/yr, hence a most likely long-term average between 2 and 3 mm/yr (Fig. 11a). Within ~20%
500 uncertainty (0.4 to 0.6 mm/yr), these rates appear to have been constant over a much longer
501 timescale (~210 ka), ~100 ka older than that documented so far. They compare well with the
502 2.6±0.5 mm/yr rate recently determined by Peltzer et al. (2020) in the last ~115 ka. Locally, the
503 total Taersa long-term rates include a vertical component (~0.1 mm/yr) that absorbs some
504 cumulative displacement. Additionally, faulting along the southern side of the pull-apart sag
505 within the Karakax valley (Fig. 2) may contribute to increase slightly the total Taersa slip rate.
506 Such consistent, ~2.5 mm/yr average rate values at three sites over a ~35 km-long stretch of
507 the fault suggest that previous estimates of rates 2 to 3 times faster (6-9 mm/yr), may have been
508 biased. Li et al.'s (2012) estimate (6-7 mm/yr) was based on just one ^{14}C date (975-1020 AD) in
509 one trench west of Taersa with no *in situ* horizontal offset measurement (Fig. 2). Gong et al.'s
510 (2017) rate (7.8±1.6 mm/yr) was derived from the OSL dating of six, reportedly fluvial, sand
511 samples (39.7±2.5 ka for T4 [their T5], 28.5±1.7 ka for T3' [their T4], 21.2±1.2 ka for T3 and
512 14.5±1.0 ka for T2) retrieved from the very top of unstable, south-facing risers, likely still
513 retreating and affected by steady, long-term rejuvenation due to ongoing erosion by the Karakax
514 river (Fig. 8a). In fact, more importantly, since the depth of these OSL samples is very shallow

(15-45 cm, Gong et al., 2017), and their ages much younger than those we obtain on all the relevant surfaces (Fig. 9), we suspect that the deposits they dated may include loess windblown atop the terrace surfaces much later than their fluvial abandonment ages.

5.3 Regular recurrence times of comparably large earthquakes along the Karakax fault

In the last 150 years, seven large (M≥7) earthquakes have struck the broad region surrounding the West Kunlun range and western branches of the Altyn Tagh fault (ATF) (Figs. 1 and 13) (SBX, 1997). The most recent (M_w 6.9, 2014 and M_w 7.2, 2008 Yutian earthquakes) ruptured the Ashikule left-lateral fault (Li et al., 2016) and the West Pingding normal fault (e.g., Xu et al., 2013), within the transition zone between the ATF and the Longmu-Gozha Co fault (LGCF). Another event (M_s 6.9 in 1996) ruptured a poorly studied, probably ~EW-striking fault within the Tianshuihai block, with a debated left-lateral or thrust mechanism (USGS; Ma et al., 1997). One century ago, in 1924, two events with estimated magnitudes of 7.2 and 7.5 (Chen, 1988) likely ruptured segments or splays of the western ATF east of Minfeng. Even earlier on, in 1882 and 1889, two large earthquakes are reported to have been strongly felt in Hotan and Yecheng, respectively (Nikonov, 1975; Ma, 1989; Avouac and Peltzer, 1993). Since little is known about these two events, however, doubts have been raised on their existence or location (Yang et al., 1991).

Yet, during our field work across the region, we found only one large, fresh surface rupture along faults in the West Kunlun range south of Hotan and Yecheng (Fig. 12). In the field and on high-resolution satellite images, this rupture (yellow swath in Fig. 1b) may be followed continuously for ~150 km, from ~77.5°E to 79°E. Where the fault is single-stranded, field

538 measurements imply an average left-lateral co-seismic displacement of 6±1 m (Li et al., 2012).
539 The facts that this rupture displays well-preserved, ~1.5 m-high, free-faces and en-echelon mole
540 tracks across the Sanshili and other fans (Li et al., 2012), that it affects the most recent terraces,
541 and that it is still visible across some of the floodplains of the Karakax tributaries (Fig. 12), are in
542 keeping with the inference that it is less than 200 years old. The measured rupture length and slip
543 amount are consistent with a magnitude M7.6 (M=5.08+1.16*log[surface rupture length=150 km]
544 or M=6.93+0.82*log[average displacement=6 m], Wells and Coppersmith, 1994). Hence, as
545 inferred by Avouac and Peltzer (1993), we conclude that this rupture is most likely that of the
546 1882 Hotan earthquake (Fig. 1b).
547

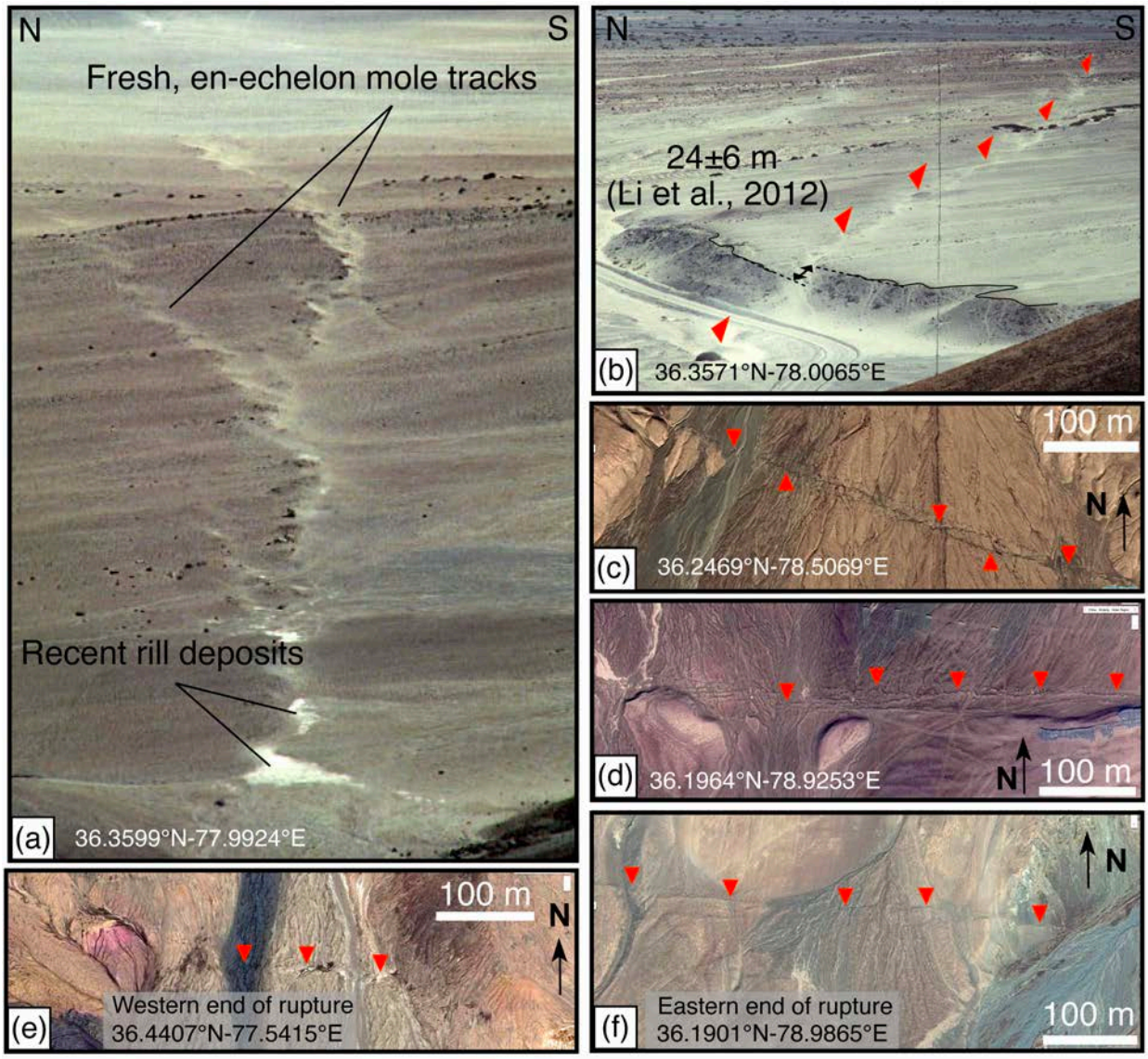

Figure 12. *Fresh surface rupture of 1882 earthquake (see image locations in Fig. 1b). (a) Field photograph (P. Tapponnier, 1989) of en-echelon, right-stepping scarps across fan south of Karakax river, west of Sanshili. Note slight vertical offset north of rupture and fresh white pluvial deposits dammed by scarp. (b) Field photograph of offset, western riser of Sanshili fan (~24±6 m) and fresh surface rupture across fan surface. Note again slight vertical offset north of fault trace. (c and d) Maxar satellite images of fresh seismic rupture across recent Karakax tributary alluvial surfaces and active seasonal streams. (e and f) Deep open cracks close to western and eastern terminations of ~150 km-long, 1882 surface rupture, respectively.*

Finally, the epicenters of one historical event and one recent earthquake both lie in the SW Tarim basin, just north of the West Kunlun range. The 2015, Mw 6.4 Pishan earthquake ruptured a blind, south-dipping thrust west of Hotan (Fig. 1a) (e.g., Lu et al., 2016; Wen et al., 2016; Guilbaud et al., 2017; Laborde et al., 2019). The poorly documented, possibly larger, 1889 event, tentatively located near Yecheng, might also have ruptured a blind thrust in the Kunlun foreland, south of the emergent, active Mazartagh thrust ramp (Fig. 13a).

The large 1882 Karakax surface break appears to be the latest in a sequence of similar ruptures with comparable amounts of co-seismic slip. Previous field measurements (Li et al., 2012) documented cumulative offset amounts of ~12, ~18 and ~24 m across four young fluvial fans along the central ~50 km of the rupture. At Taersa, our new Matlab measurements confirm values of ~6, ~13, ~18 and ~23 m across the lowermost, Holocene (10±2 ka), alluvial terraces (Fig. 3e). The ~2.5±0.5 mm/yr slip rate at this site would thus be consistent with characteristic slip (~6 m) event's return times of ~2500±500 years (Fig. 11c). Note that such long recurrence times preclude the use of historical records to assess seismic hazard on the fault. The rare preservation of four cumulative co-seismic offsets over the entire Holocene period yields a characteristic slip record that would be hard to obtain from trenching, even where sedimentary records reach back that long (e.g., Daëron et al., 2007).

5.4 Slip-rate along the Karakax fault at the millennial timescale

The ~210 ka, 2-3 mm/yr slip rate we obtain is slower than average rates estimated geodetically across the West Kunlun range during the last ~20 years: e.g., 7±3 mm/yr (GPS, Shen et al., 2001), 5±5 mm/yr (Interferometric Synthetic Aperture Radar [InSAR], Wright et al.,

2004). As discussed below, this may be a corollary consequence of the complex crustal deformation and faulting geometry across the western tip of Tibet (Figs. 1 a and 13a).

On a long-term, geological timescale, matching the Karakax river ~80 km offset (Gaudemer et al., 1989, Ding et al., 2004) with the likely onset age (≥24 Ma) of rapid sedimentation in the Tarim basin's Kunlun foreland and of sustained tectonic uplift along the West Kunlun range (e.g., Matte et al., 1996; Sobel and Dumitru, 1997; Métivier et al., 1999; Cao et al., 2015), would yield a long-term slip rate of ≤3.3 mm/yr, consistent, within uncertainties, with the average late Quaternary rate we document here. The similar ~80 km offset of the neighboring Karakax and Yurungkax, two comparably large rivers crossing the KXF across nearly impassable gorges/canyons (Fig. 1a), have long been described and clearly attributed to sinistral movement along the fault (e.g., Gaudemer et al., 1989; Ding et al., 2004). The two river floodplains are, and must have long been, captive within their deeply incised passages across mountain ranges that are now 6000 to 7000 m-high. That the highest Kunlun peaks NW and SE of the offset Karakax river are ~6300 and ~6698 m-high, i.e., ~2600 m and ~3000 m above the present valley floor (~3700 m), respectively (Fig. 1b), requires that these large offsets be nearly coeval with the onset of mountain uplift.

The ~24 Ma, ~210 ka, ~110 ka, and ~10 ka slip rates along the Karakax splay of the ATF would thus all fall between 2 and 3.3 mm/yr, in keeping with a long (~2500 years) return time for M~7.6 earthquakes and a total, post-early Miocene offset of ~80 km. That relatively slow rate is surprising given the clear, continuous surface trace, the fairly large co-seismic and geological offsets, the prominent ~150 km-long 1882 surface rupture, and the exceptionally well-preserved geomorphic expression of the fault (Fig. 12). Peltzer et al. (2020) suggested that variable slip or erosion rates might account for the non-linear relationship between progressive scarp

603 degradation and cumulative displacement along the fault. Our results tend to support the latter,
604 although complexities in the fault trace involving pull-apart sags and releasing bends, hence sub-
605 parallel surface strands, in part hidden within the fast-evolving, modern Karakax river floodplain,
606 likely play a significant role.
607
608 **5.5 Left-lateral slip rate along the Longmu Co fault**
609 While we do not provide here more local dates along the Longmu Co fault (southern branch
610 of the LGCF) south of the Sumxi-Longmu Lakes, the offsets shown in Figure 4 (32±4 and
611 950±50 m) are newly-derived from a dedicated, small-scale UAV survey and from recent (2021)
612 high-resolution "Maxar Technology" satellite images, respectively. Age constraints for these two
613 different cumulative offsets may be suitably deduced from reliable, published, local and regional
614 dating by Gasse et al. (1991), Avouac et al. (1996), and Amidon et al. (2013). The twin Sumxi
615 and Longmu Lakes were long-connected as a unique, large lake with maximum water heights at
616 least ~230 m above present level (Avouac et al., 1996) during the early HCO (~10 to ~5 ka,
617 Gasse et al., 1991). The 32±4 m left-lateral offset of the topmost shoreline of the paleo-Sumxi-
618 Longmu Lake must post-date the abandonment of that shoreline as the lake level rapidly dropped
619 down at the end of the HCO (6-5.5 ka, Avouac et al., 1996). This implies a slip rate on the
620 Longmu Co fault of 5.6±0.9 mm/yr (Fig. 11b).
621 The larger offsets (~950±50 m) of the narrow glacial streams, now captive within the
622 abandoned glacial valleys crossing the fault south of the lakes, likely post-date the MIS-6 glacial
623 maximum (~180-140 ka, Fig. 9), after which incision began, a timing in keeping with the age of
624 the oldest, recessional frontal moraine (34.414°N-80.046°E) dated at 123±5 ka by Amidon et al.
625 (2013). Note that this moraine is located only ~21 km southwest of the offset shoreline site (Fig.

626 4) and ~8 km due south of the westernmost abandoned shorelines of Sumxi-Longmu Lake
627 (Avouac et al., 1996). Assuming that the glacial valley offsets post-date glacial retreat (e.g.,
628 Chevalier et al., 2005), between ~150 and 140 ka, their 950±50 m average sinistral offset would
629 imply a slip rate of 6.5±0.4 mm/yr (Fig. 11a). We conclude that the slip rate along the Longmu
630 Co fault may be significantly faster than the value proposed by Chevalier et al. (2017) (<3 mm/yr
631 at a site located ~15 km west of the offset shoreline above), that may have been biased by the
632 ages of cobbles transported downstream by post-glacial reworking of upstream moraine deposits.
633 Note that the two rate values derived here along the central Longmu Co fault south of Lake
634 Sumxi are within the range of those inferred at various timescales by Raterman et al. (2007).
635

636 **5.6 Large-scale slip partitioning, triple junction kinematics and crustal**
637 **block tectonics across western Tibet**

638 Earlier studies along the ATF suggested Quaternary slip rates of up to 20-30 mm/yr (e.g.,
639 Molnar et al., 1987; Molnar and Lyon-Caen, 1989; Peltzer et al., 1989; Mériaux et al., 2004,
640 2005; Ryerson et al., 2006), the latter three at specific field sampling sites along the central and
641 eastern ATF. While local rates ≥20 mm/yr have been disputed, rates between ~10 and 15 mm/yr
642 along the fault from ~84 to 93°E are now well-established over different timescales (e.g., Gold et
643 al., 2011; Mériaux et al., 2012; Daout et al., 2018 and references therein). How rates ≥10 mm/yr
644 on the central ATF decrease to only 2-3 mm/yr in the Karakax valley must be accounted for. The
645 most plausible reason is the westward increasing complexity of the ATF system. While relatively
646 linear, although segmented into parallel strands by releasing and restraining bends east of 84°E,
647 the fault partitions westwards into distinct branches separating rising mountains from broad
648 basins (Figs. 1 a and 13a). Whereas it is essential to assess crustal kinematics across western

649 Tibet, such splitting into splays with strike-slip, thrust or normal components remains to be
650 accurately quantified.

651 The central ATF divides into two main faults (KXF and LGCF) at the Uzatagh triple junction
652 (83°E, Fig. 13a). Near that junction, where the strike of the KXF starts veering northwards by
653 ~40°, the sub-parallel Pishan-Kashitashi thrust, which raises the West Kunlun range to maximum
654 elevations of ~6000-6700 m, also terminates. A similar ~40° clockwise turn occurs near 81°E in
655 the Tarim foreland, between the emergent Minfeng-Cherchen sliver- and Mazar Tagh thrusts,
656 that parallel the ATF and KXF, respectively. We thus interpret the ~NE-striking, dominantly
657 normal, Qira fault zone (Avouac and Peltzer, 1993), to merge with both the Minfeng-Cherchen
658 sliver thrust and a ~NS-striking ramp bounding the eastern side of the Mazar Tagh thrust sheet.
659 Such a connection, near Qira, may be regarded as another triple junction (Damagou junction,
660 Fig. 13a). Southwest of Uzatagh, the ATF splits into a complex pull-apart system with oblique
661 sinistral/normal branches that merge back again southwestwards into the left-stepping LGCF
662 (Figs. 1 a and 13a). While the M~7, 2008 and 2014 Yutian earthquakes ruptured the
663 northwestern (West Pingding and Ashikule-Xor Kol) branches of that system, no large event has
664 been recorded yet along the southeastern branch, although it follows a deep, active rift between
665 the highest mountains (>6900-7100 m) of the West Kunlun range (Fig. 13a). Finally, farther SW,
666 the Longmu Co fault merges with the southern and northern Karakorum faults at the Angmong
667 triple junction, which also marks the southern termination of the high Karakorum range (Fig.
668 13a), where >40 km of post-Miocene crustal heave has occurred (Van Buer et al., 2015).
669

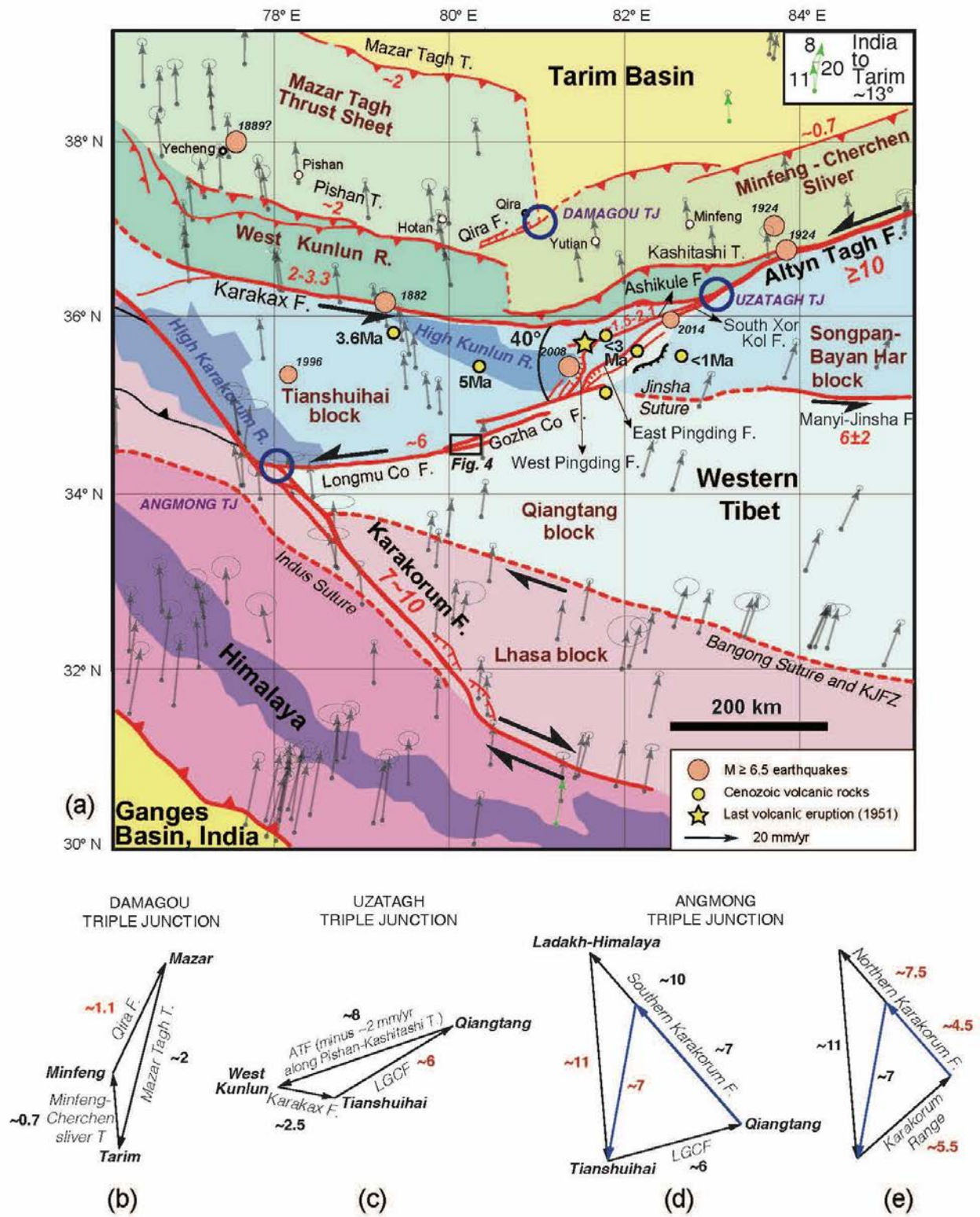

670

671 ***Figure 13.*** *Block tectonics model consistent with updated fault slip rates across western Tibet. (a)*

672 *Summary of late Quaternary slip rates (numbers in red, in mm/yr) along main active faults (F.,*

673 *red lines) and thrusts (T., red lines with teeth) separating crustal blocks between India and*
674 *Tarim (colored, after Wittlinger et al., 2004), with GPS vectors (small arrows) relative to stable*
675 *Eurasia (Wang and Shen, 2020). Large blue circles are three main triple junctions (TJ). Dark*
676 *blue/purple polygons highlight the highest topography along the Kunlun, Karakorum and*
677 *Himalayan ranges (R.). Small black box along LGCF indicates location of Figure 4. (b-e)*
678 *Triangular diagrams consistent with vector sums of late Quaternary slip rates along faults*
679 *separating blocks around triple junctions (red numbers are predicted rates; see discussion in*
680 *text). Top right inset is triangular diagram between current GPS vectors (green) just north of*
681 *Himalaya and in Tarim basin.*
682

683 While few long-term slip rates are well-constrained except along the ATF-KXF and
684 Karakorum faults, InSAR measurements now reveal ~0.7 mm/yr of ~NS shortening across the
685 Minfeng-Cherchen thrust and 6±2 mm/yr of ~EW sinistral motion along the western Manyi-
686 Jinsha fault (Daout et al., 2018) (Fig. 13a). Field studies imply ~NS shortening rates of ~2-2.5
687 and ~1.5-2.5 mm/yr across the Pishan and Mazar Tagh thrusts, respectively (Guilbaud et al.,
688 2017; Laborde et al., 2019). If assumed constant since shortening began in the West Kunlun
689 range (~24 Ma), the sum of the latter rates (~3.5-5 mm/yr) would be consistent with subduction
690 of the Tarim lithospheric mantle to a depth of ~200 km (88-125 km beneath the ~90 km depth of
691 the west Tibetan Moho) (Lyon-Caen and Molnar, 1984; Wittlinger et al., 2004), in classic plate
692 tectonic behavior, coherent with young volcanism south of the West Kunlun range (small yellow
693 circles in Fig. 13a). Lastly, along the Ashikule fault, cosmogenic dating of terrace offsets
694 suggests rates of ~1.5-2.1 mm/yr (Pan et al., 2015) (Fig. 13a).
695 Kinematic triangular diagrams (Fig. 13b-e) fitting the vector sums of rates along the faults
696 that separate the seven west-Tibetan blocks (Tarim, Mazar, Minfeng, Qiangtang, West Kunlun,
697 Tianshuihai, Ladakh-Himalaya; color-coded in Fig. 13a), which appear to take up much more
698 seismic strain than does internal deformation, clearly support block tectonics (e.g., Meyer et al.,

699 1998; Raterman et al., 2007). Specifically, at the Damagou junction, divergent thrusting on the
700 Mazar Tagh and Minfeng thrusts results in ~1.1 mm/yr of ~NNE extension along the Qira fault
701 zone (Fig. 13b). The decrease in sinistral rate between the ATF and KXF is consistent with
702 transfer, at the Uzatagh junction, of ~6 mm/yr of slip along the LGCF (Fig. 13c) in a direction
703 enabling extension along the eastern boundary of the West Kunlun range. That rate is consistent
704 with both the 32±4 m offset of the Sumxi-Longmu Lake topmost shoreline, abandoned ~6-5.5 ka
705 ago (Gasse et al., 1991; Avouac et al., 1996) and the larger offsets (950±50 m) of Eemian (123±5
706 ka, Amidon et al., 2013) glacial valleys (Fig. 4). Finally, the vector sum of rates along the
707 southern Karakorum (~10 mm/yr, Chevalier et al., 2005) and LGCF (~6 mm/yr) predicts ~11
708 mm/yr of ~NS shortening west of the Angmong junction (Fig. 13d). This may be further
709 decomposed into ~4.5-7.5 mm/yr of dextral motion along the northern Karakorum fault and ~5.5
710 mm/yr of shortening across the high Karakorum range (Fig. 13e). Note that a faster dextral slip
711 rate along the central Karakorum fault is consistent with very short-term InSAR geodetic
712 observation (Wang and Wright, 2012). Most importantly, the kinematics of the latter, Angmong
713 junction, would thus account for the rise of the second highest mountain range in Asia after the
714 central Himalayas. The dextral rate decrease and the glaciated, high topography past that
715 junction would explain why the active Karakorum fault was mistakenly inferred by some (e.g.,
716 Robinson, 2009) to terminate north of ~34°N.

717 Detailed field studies are still lacking in the region separating the Himalayas from the Tarim
718 basin. Active faults that might bound the steep SW and NE faces of the West Kunlun and
719 Karakorum ranges (dark blue patches in Fig. 13a), contributing to the deformation budget across
720 the plateau, remain unexplored. This notwithstanding, however, a pattern of regional
721 deformation dominated by block faulting seems to be inescapable. Triple junction-governed slip-

partitioning, similar to that long-successful in plate tectonics (e.g., McKenzie and Morgan, 1969), appears to account best for changes in slip rates at the merging points between the central ATF, KXF and LGCF, southern and northern Karakorum and Longmu Co faults, and between the Qira fault, Mingfeng-Cherchen and Mazar Tagh thrusts (Fig. 13a). Likewise, the fact that the highest mountains in western Tibet abruptly terminate near two of these junctions is best explained by triple junction kinematics. Stronger crustal shortening, accounting for both the maximum elevations of the Karakorum range and northwestward right-lateral slip decrease along the eponymous fault (Chevalier et al., 2016), may just be interpreted as a simple consequence of such kinematics. While the current, local geodetic dataset remains insufficient, both space- and time-wise, to fully corroborate block tectonics, the main amplitude and directional changes of extant GPS vectors (a total of ~13° anticlockwise, top right inset in Fig. 13a, Wang and Shen, 2020) between the Himalaya and the Tarim tend to coincide with the positions of the main active faults. That several of the largest faults follow ancient, likely weak, crustal/lithospheric divides between the main terranes of the Tibetan collage (e.g., Oytag, Jinsha and Bangong sutures, Matte et al., 1996; Wittlinger et al., 2004), mechanically justifies the observed behavior. Crucially, while complex, the late Quaternary kinematics across western Tibet strongly support simple block tectonics rather than broadly diffuse deformation (Peltzer and Tapponnier, 1988; Meyer et al., 1998; Tapponnier et al., 2001; Loveless and Meade, 2011).

6 Conclusion

New slip rate measurements along the Karakax and Longmu Co faults, westernmost branches of the Altyn Tagh fault, help understand broad-scale block kinematics across the western tip of the Tibetan Plateau, between the Ganges plain and the Tarim basin. Over the last

745 ~210 ka (age of the oldest alluvial surface dated thus far in northwestern Tibet), and possibly
746 since ~24 Ma, the slip rate along the Karakax fault seems to have remained constant, between 2
747 and 3 mm/yr, as recently shown by Peltzer et al. (2020) since ~115 ka. Since the beginning of the
748 Holocene, great earthquakes (M~7.6) appear to have ruptured at least ~150 km of the fault with
749 fairly regular, if long (~2500±500 years) return times, and with characteristic co-seismic slip
750 amounts on order of 6 m - as was the case for the last, likely 1882 AD event - for four such
751 events. These conclusions are based on the combination of high-resolution digital elevation
752 surveys and dating of alluvial fan and terrace offsets at Taersa in the Karakax valley, and of lake
753 shoreline and glacial valley offsets by the Longmu Co fault south of Sumxi Lake. Along the
754 Karakax fault, the well-known, ~80 km offset of the Karakax river may have accrued since uplift
755 of the West Kunlun range started in the early Miocene (~24 Ma). The sum of the slip rates on the
756 Longmu Co fault (~6 mm/yr) with those on the Karakax fault (~2-3 mm/yr) and on the active
757 thrusts (2x~2 mm/yr = ~4 mm/yr) along the Tarim foreland of the Kunlun, yields a total of ≥12
758 mm/yr along the central Altyn Tagh fault, between central Tibet and the Tarim, in keeping with
759 the modern InSAR rate (≥10.5 mm/yr) obtained by Daout et al. (2018). To a first order, at the
760 scale of the entire western plateau, block tectonics and triple junction kinematics appear to
761 account for the recent and late Tertiary continental deformation, even though the seven blocks
762 involved, particularly the Tianshuihai block, may not be torsionally rigid. Specifically, the
763 junction between the conjugate Longmu Co and Karakorum strike-slip faults may be key to
764 explain the rise and abrupt southern termination of the high Karakorum range, second highest in
765 the world. Our results bridge the gaps between present and long-term geological history, and
766 between broad-scale geodesy and local field evidence.
767

Acknowledgments and Data

This work was supported by the 2nd Tibetan Plateau Scientific Expedition of the Ministry of Science and Technology of China (2019QZKK0901), the National Natural Science Foundation of China (41672211, 41941016), the China Geological Survey (DD20190059), the Basic Research Funds of the Institute of Geology, Chinese Academy of Geological Sciences (JYYWF201810), and Key Special Project for Introduced Talents Team of Southern Marine Science and Engineering Guangdong Laboratory (Guangzhou) (GML2019ZD0201). The first exploratory 1989 field trip was funded by INSU-CNRS, the French Ministry of Research and Higher Education and the Chinese Academy of Geological Sciences (CAGS). The 1995 field work was supported by a NASA SIC-C investigation. LLNL's participation in the 1995 sampling trip as well as cosmogenic dating of those 1995 samples were supported by the Laboratory Directed Research Project (01-ERI-009) at Lawrence Livermore National Laboratory operating under the auspices of the US Department of Energy by Lawrence Livermore National Laboratory under Contract DE-AC52-07NA27344. Dating at the ASTER AMS French national facility (CEREGE, Aix-en-Provence) was supported by the INSU-CNRS, the French Ministry of Research and Higher Education, IRD, and CEA. We thank J.P. Avouac for his participation in the 1989 field expedition, and M. Bai for his help with the LiDAR processing and Matlab run. We thank the Editor, Associate Editor, and two anonymous reviewers for their constructive comments. Ages and digital elevation surveys (LiDAR and UAV) data are available at https://zenodo.org/record/5115549#.YPjRpC0RrjA.

References

790 Amidon, W. H., Bookhagen, B., Avouac, J. P., Smith, T., & Rood, D. (2013), Late Pleistocene
791 glacial advances in the western Tibet interior. *Earth and Planetary Science Letters, 381*, 210-
792 221. https://doi: 10.1016/j.epsl.2013.08.041.
793 Armijo, R., Tapponnier, P., & Han, T. (1989), Late Cenozoic right-lateral strike-slip faulting in
794 southern Tibet. *Journal of Geophysical Research Solid Earth, 94(*B3), 2787-2838.
795 https://doi.org/10.1029/JB094iB03p02787.
796 Avouac, J. P., & Peltzer, G. (1993), Active tectonics in southern Xinjiang, China: Analysis of
797 terrace riser and normal fault scarp degradation along the Hotan-Qira fault system. *Journal of*
798 *Geophysical Research Solid Earth, 98(*B12),773-807. https://doi.org/10.1029/93JB02172.
799 Avouac, J. P., & Tapponnier, P. (1993), Kinematic model of active deformation in central Asia.
800 *Geophysical Research Letters, 20*(10), 895–898. https://doi.org/10.1029/93GL00128.
801 Avouac, J. P., Dobremez, J. F., & Bourjot, L. (1996), Palaeoclimatic interpretation of a
802 topographic profile across middle Holocene regressive shorelines of Longmu Co (Western
803 Tibet). *Palaeogeography Palaeoclimatology Palaeoecology, 120*, 93-104.
804 https://doi.org/10.1016/0031-0182(96)88700-1.
805 Balco, G., Stone, J. O., Lifton, N. A., & Dunai, T. J. (2008), A complete and easily accessible
806 means of calculating surface exposure ages or erosion rates from ^{10}Be and ^{26}Al
807 measurements. *Quaternary Geochronology, 3*(3), 174-195.
808 Doi:10.1016/j.quageo.2007.12.001.
809 Bevington, P.R., & Robinson, D.K. (2002), Data Reduction and Error Analysis for the
810 Physical Sciences, 336 pp., McGraw-Hill, New York.
811 Blisniuk, P. M., & Sharp, W. D. (2003). Rates of late Quaternary normal faulting in central Tibet from
812 U□series dating of pedogenic carbonate in displaced fluvial gravel deposits. *Earth and Planetary*
813 *Science Letters*, 215(1–2), 169–186.

814 Brown, E. T., Bendick, R., Bourlès, D. L., Gaur, V., & Yiou, F. (2003), Early Holocene climate recorded
815 in geomorphological features in Western Tibet. *Palaeogeography Palaeoclimatology*
816 *Palaeoecology, 199*(1), 141-151. https://doi.org/10.1016/S0031-0182(03)00501-7.
817 Cao, K., Wang, G. C., Bernet, M., van der Beek, P., & Zhang, K. X. (2015), Exhumation history
818 of the West Kunlun Mountains, northwestern Tibet: Evidence for a long-lived, rejuvenated
819 orogen. *Earth and Planetary Science Letters, 432*, 391-403. Doi:10.1016/j.epsl.2015.10.033.
820 Chen, X. (1988), Xinjiang earthquake catalogue (ms ≥ 4.7) from 1600 to 1987. *Inland*
821 *Earthquakes, 3,* 320-340. https://doi:10.16256/j.issn.1001-8956.1988.03.016
822 Chevalier, M. L., Ryerson, F. J., Tapponnier, P., Finkel, R. C., Van der Woerd, J., Li, H., & Liu,
823 Q. (2005), Slip-rate measurements on the Karakorum Fault may imply secular variations in
824 fault motion. *Science, 307*(5708), 411-414. https://doi:10.1126/science.1105466.
825 Chevalier, M. L., Van der Woerd, J., Tapponnier, P., Li, H., Ryerson, F. J., & Finkel, R. C.
826 (2016), Late Quaternary slip-rate along the central Bangong-Chaxikang segment of the
827 Karakorum fault, western Tibet. *Geological Society of America Bulletin, 128*(1-2), 284-314.
828 https://doi:10.1130/b31269.1.
829 Chevalier, M. L., Pan, J., Li, H., Sun, Z., Liu, D., Pei, J., et al. (2017). First tectonic-
830 geomorphology study along the Longmu-Gozha Co fault system, Western Tibet. *Gondwana*
831 *Research, 41*, 411-424. https://doi:10.1016/j.gr.2015.03.008.
832 Cowgill, E. (2007), Impact of riser reconstructions on estimation of secular variation in rates of
833 strike-slip faulting: Revisiting the Cherchen River site along the Altyn Tagh Fault, NW
834 China. *Earth and Planetary Science Letters, 254*(3–4), 239–255.
835 doi:10.1016/j.epsl.2006.09.015.

836 Daëron, M., Klinger, Y., Tapponnier, P., Elias, A., Jacques, E., & Sursock, A. (2007), 12,000-
837 year-long record of 10 to 13 paleoearthquakes on the Yammouneh fault, Levant fault system,
838 Lebanon. *Bulletin of the Seismological Society of America, 97*(3), 749-771.
839 https://doi:10.1785/0120060106.
840 Daout, S., Doin, M. P., Peltzer, G., Lasserre, C., Socquet, A., Volat, M., & Sudhaus, H. (2018),
841 Strain partitioning and present□day fault kinematics in NW Tibet from Envisat SAR
842 interferometry. *Journal of Geophysical Research, 123*(3), 2462-2483.
843 https://doi:10.1002/2017jb015020.
844 DeMets, C., Gordon, R. G., Argus, D., & Stein, S. (1990), Current plate motions. *Geophysical*
845 *journal international, 101(*2), 425-478. https://doi.org/10.1111/j.1365-246X.1990.tb06579.x.
846 Ding, G., Chen, J., Tian, Q., Shen, X., Xing, C., & Wei, K. (2004), Active faults and magnitudes
847 of left-lateral displacement along the northern margin of the Tibetan Plateau. *Tectonophysics,*
848 *380(*3-4), 243-260. Doi:10.1016/j.tecto.2003.09.022.
849 Farr, T., & Chadwick, O. (1996). Geomorphic processes and remote sensing signatures of
850 alluvial fans in the Kunlun Mountains, China. *Journal of Geophysical Research,*
851 *101(*E10), 23,091-23,100.
852 Gasse, F., Téhet, R., Durand, A., Gibert, E., & Fontes, J. C. (1990), The arid–humid transition in
853 the Sahara and the Sahel during the last deglaciation. *Nature*, *346*(6280), 141-146.
854 Gasse, F., Arnold, M., Fontes, J. C., Fort, M., Gibert, E., Huc, A. et al. (1991), A 13,000-year
855 climate record from western Tibet. *Nature*, *353*(6346), 742-745. https://doi:
856 10.1016/j.tecto.2003.09.022.
857 Gaudemer, Y., Tapponnier, P., & Turcotte, D. (1989), River offsets across active strike-slip
858 faults. *Annales Tectonicae, 3,* 55–76.

859 Gold, R. D., Cowgill, E., Arrowsmith, R., Gosse, J., Chen, X., & Wang, X. (2009). Riser
860 diachroneity, lateral erosion, and uncertainty in rates of strike-slip faulting: A case
861 study from Tuzidun along the Altyn Tagh Fault, NW China. *Journal of Geophysical*
862 *Research, 114*(B04401), 1–24. https://doi.org/10.1029/2008JB005913
863 Gold, R. D., Cowgill, E., Arrowsmith, J. R., Chen, X., Sharp, W. D., Cooper, K. M., & Wang, X.
864 (2011), Faulted terrace risers place new constraints on the late Quaternary slip rate for the
865 central Altyn Tagh fault, northwest Tibet. *Geological Society of America Bulletin, 123(*5-6),
866 958-978. https://doi.org/10.1130/B30207.1.
867 Gong, Z., Sun, J., Zhang, Z., Fu, B., & Jia, Y. (2017), Optical dating of an offset river terrace
868 sequence across the Karakax fault and its implication for the late Quaternary left-lateral slip
869 rate. *Journal of Asian Earth Sciences, 147,* 415-423.
870 https://doi.org/10.1016/j.jseaes.2017.07.013.
871 Guilbaud, C., Simoes, M., Barrier, L., Laborde, A., Van der Woerd, J., Li, H. et al. (2017),
872 Kinematics of active deformation across the Western Kunlun mountain range (Xinjiang,
873 China) and potential seismic hazards within the southern Tarim Basin. *Journal of*
874 *Geophysical Research, 122*(12), 10,398-426. Doi:10.1002/2017JB014069.
875 Hetzel, R., Niedermann, S., Tao, M.X., Kubik, P.W., Ivy-Ochs, S., Gao, B., Strecker, M.R.,
876 (2002), Low slip rates and long-term preservation of geomorphic features in Central
877 Asia. *Nature, 417,* 428–432.
878 Hidy, A. J., Gosse, J. C., Pederson, J. L., Mattern, J. P., & Finkel, R. C. (2010), A geologically
879 constrained Monte Carlo approach to modeling exposure ages from profiles of cosmogenic
880 nuclides: An example from Lees Ferry, Arizona. *Geochemistry, Geophysics, Geosystems,*
881 *11*(9) ,1-18. https://doi:10.1029/2010gc003084.

882 Kohl, C. P., & Nishiizumi, K. (1992), Chemical isolation of quartz for measurement of in-situ
883 produced cosmogenic nuclides. *Geochimica et Cosmochimica Acta, 56(*9), 3583-3587.
884 https://doi.org/10.1016/0016-7037(92)90401-4.
885 Laborde, A., Barrier, L., Simoes, M., Li, H., Coudroy, T., Van der Woerd, J., & Tapponnier, P.
886 (2019), Cenozoic deformation of the Tarim Basin and surrounding ranges (Xinjiang, China):
887 A regional overview. *Earth Science Reviews, 197*, 102891.
888 https://doi:10.1016/j.earscirev.2019.102891.
889 Lal, D. (1991), Cosmic ray labeling of erosion surfaces: in situ nuclide production rates and
890 erosion models. *Earth and Planetary Science Letters, 104*(2-4), 424-439.
891 https://doi:10.1016/0012-821x(91)90220-c.
892 Li, H., Van Der Woerd, J., Tapponnier, P., Yann, K., Qi, X., Yang, J., & Zhu, Y. (2005), Slip
893 rate on the Kunlun fault at Hongshui Gou, and recurrence time of great events comparable to
894 the 14/11/2001, Mw7.9 Kokoxili earthquake. *Earth and Planetary Science Letters, 237*(1-2),
895 285-299. https://doi.org/10.1016/j.epsl.2005.05.041.
896 Li, H., Van Der Woerd, J., Sun, Z., Si, J., Tapponnier, P., Pan, J. et al. (2012), Co-seismic and
897 cumulative offsets of the recent earthquakes along the Karakax left-lateral strike-slip fault in
898 western Tibet. *Gondwana Research, 21*(1), 64-87. https://doi:10.1016/j.gr.2011.07.025.
899 Li, H., Pan, J., Lin, A., Sun, Z., Liu, D., Zhang, J. et al. (2016), Coseismic Surface Ruptures
900 Associated with the 2014Mw 6.9 Yutian Earthquake on the Altyn Tagh Fault, Tibetan
901 Plateau. *Bulletin of the Seismological Society of America,106*, 595–608.
902 https://doi:10.1785/0120150136.

903 Lifton, N., Sato, T., & Dunai, T. J. (2014), Scaling in situ cosmogenic nuclide production rates
904 using analytical approximations to atmospheric cosmic-ray fluxes. *Earth and Planetary*
905 *Science Letters, 386*, 149-160. https://doi:10.1016/j.epsl.2013.10.052.
906 Lisiecki, L. E., & Raymo, M. E. (2005), A Pliocene□Pleistocene stack of 57 globally distributed
907 benthic $\delta^{18}O$ records. *Paleoceanography, 20*(1), 1-17. https://doi:10.1029/2004pa001071.
908 Liu, Q. (1993), Paleoclimat et contraintes chronologiques sur les mouvements récents dans
909 l'Ouest du Tibet: failles du Karakorum et de Longmu Co-Gozha Co, lacs en pull-apart de
910 Longmu Co et de Sumxi Co, (Doctoral dissertation). Université de Paris VII.
911 Loveless, J. P., & Meade, B. J. (2011), Partitioning of localized and diffuse deformation in the
912 Tibetan Plateau from joint inversions of geologic and geodetic observations. *Earth and*
913 *Planetary Science Letters, 303*(1-2), 11-24. https://doi: 10.1016/j.epsl.2010.12.014.
914 Lu, R., Xu, X., He, D., Liu, B., Tan, X., & Wang, X. (2016), Coseismic and blind fault of the
915 2015 Pishan Mw 6.5 earthquake: Implications for the sedimentary□tectonic framework of
916 the western Kunlun Mountains, northern Tibetan Plateau. *Tectonics, 35*(4), 956-964.
917 https://doi:10.1002/2015tc004053.
918 Lyon□Caen, H., & Molnar, P. (1984), Gravity anomalies and the structure of western Tibet and
919 the southern Tarim Basin. *Geophysical Research Letters, 11(*12), 1251-1254.
920 https://doi.org/10.1029/GL011i012p01251.
921 Ma, X. (Eds.) (1989), Seismotectonic map of xinjiang, lithospheric dynamics atlas of china.
922 *China cartographic publishing house.*
923 Ma, S., Yao, Z., & Ji, C. (1997), The Focal Mechanism Solution for March 19, 1996 M~ s 6.9
924 Earthquake in XinJiang Jia-Shi Region and Related Problems. *Acta Geophysica Sinica, 40,*
925 789-800.

926 Matte, P., Tapponnier, P., Arnaud, N., Bourjot, L., Avouac, J., Vidal, P. et al. (1996), Tectonics
927 of Western Tibet, between the Tarim and the Indus. *Earth and Planetary Science Letters,*
928 *142*(3-4), 311-330. https://doi:10.1016/0012821x(96)00086-6.
929 McKenzie, D.P., & Morgan, W.J. (1969), Evolution of triple junctions. *Nature, 224*, 125–133,
930 doi:10.1038/224125a0.
931 Mériaux, A. S., Ryerson, F., Tapponnier, P., Van der Woerd, J., Finkel, R., Xu, X., Xu, Z., &
932 Caffee, M. (2004), Rapid slip along the central Altyn Tagh Fault: morphochronologic
933 evidence from Cherchen He and Sulamu Tagh. *Journal of Geophysical Research, 109(*B6),
934 1-23. Doi:10.1029/2003jb002558.
935 Mériaux, A. S., Tapponnier, P., Ryerson, F. J., Xu, X., King, G., van der Woerd, J., et al. (2005).
936 The Aksay segment of the northern Altyn Tagh fault: Tectonic geomorphology,
937 landscape evolution, and Holocene slip rate. *Journal of Geophysical Research, 110*,
938 B04404. https://doi.org/10.1029/2004JB003210
939 Mériaux, A. S., Van der Woerd, J., Tapponnier, P., Ryerson, F., Finkel, R., Lasserre, C., & Xu,
940 X. (2012), The Pingding segment of the Altyn Tagh Fault (91° E): Holocene slip□rate
941 determination from cosmogenic radionuclide dating of offset fluvial terraces. *Journal of*
942 *Geophysical Research, 117*(B9). https://doi:10.1029/2012jb009289.
943 Métivier, F., Gaudemer, Y., Tapponnier, P., & Klein, M. (1999), Mass accumulation rates in
944 Asia during the Cenozoic. *Geophysical Journal International, 137*(2), 280-318.
945 https://doi.org/10.1046/j.1365-246X.1999.00802.x.
946 Meyer, B., Tapponnier, P., Gaudemer, Y., Peltzer, G., Guo, S. & Chen, Z. (1996), Rate of left-
947 lateral movement along the easternmost segment of the Altyn Tagh fault, east of 96"E
948 (China). *Geophysical Journal International, 124,* 29-44.

949 Meyer, B., Tapponnier, P., Bourjot, L., Metivier, F., Gaudemer, Y., Peltzer, G. et al. (1998),
950 Crustal thickening in Gansu-Qinghai, lithospheric mantle subduction, and oblique, strike-slip
951 controlled growth of the Tibet plateau. *Geophysical Journal International, 135*(1), 1-47.
952 https://doi.org/10.1046/j.1365-246X.1998.00567.x.
953 Molnar, P., & Lyon-Caen, H. (1989), Fault plane solutions of earthquakes and active tectonics of
954 the Tibetan Plateau and its margins. *Geophysical Journal International, 99*(1), 123-153.
955 https://doi.org/10.1111/j.1365-246X.1989.tb02020.x.
956 Molnar, P., Burchfiel, B. C., Liang, K., & Zhao, Z. (1987), Geomorphic evidence for active
957 faulting in the Altyn Tagh and northern Tibet and qualitative estimates of its contribution to
958 the convergence of India and Eurasia. *Geology, 15*(3), 249-253.
959 https://doi.org/10.1130/0091-7613(1987)15.
960 Nikonov, A. A. (1975), Migration of strong earthquakes along the greatest zones of faults in
961 Central Asia. *Doklady Akademii Nauk, 225(2),* 306–309.
962 Pan, J., Li, H., Van Der Woerd, J., Sun, Z., Si, J., Pei, J. et al. (2015), The first quantitative slip-
963 rate estimated along the Ashikule Fault at the western segment of the Altyn Tagh Fault
964 System. *Acta Geologica Sinica (English Edition), 89(*6), 2088-2089.
965 https://doi:10.1111/1755-6724.12621.
966 Peltzer, G., & Tapponnier, P. (1988), Formation and evolution of strike-slip faults, rifts, and
967 basins during the India-Asia collision; an experimental approach. J*ournal of Geophysical*
968 *Research, 93*, 15,085–15,117.
969 Peltzer, G., Tapponnier, P., & Armijo, R. (1989), Magnitude of Late Quaternary Left-Lateral
970 Displacements Along the North Edge of Tibet. *Science, 246*(4935), 1285-1289.
971 https://doi:10.1126/science.246.4935.1285.

Peltzer, G., Brown, N. D., Mériaux, A. S., van der Woerd, J., Rhodes, E. J., Finkel, R. C. et al. (2020), Stable rate of slip along the Karakax Section of the Altyn Tagh Fault from observation of interglacial and postglacial offset morphology and surface dating. *Journal of Geophysical Research: Solid Earth, 125*(5). https://doi:10.1029/2019jb018893.

Raterman, N. S., Cowgill, E., & Lin, D. (2007), Variable structural style along the Karakoram fault explained using triple-junction analysis of intersecting faults. *Geosphere, 3(*2), 71-85. https://doi:10.1130/ges00067.1.

Robinson, A. C. (2009), Evidence against Quaternary slip on the northern Karakorum Fault suggests kinematic reorganization at the western end of the Himalayan–Tibetan orogen. *Earth and Planetary Science Letters, 286*(1-2), 158-170. https://doi:10.1016/j.epsl.2009.06.025.

Ryerson, F., Peltzer, G., Tapponnier, P., Finkel, R., Mériaux, A., Van der Woerd, J., & Caffee, M. (1999), Active slip-rates on the Altyn Tagh Fault–Karakax Valley segment: Constraints from surface exposure dating. *Eos Trans. AGU, 80*(46), 1008.

Ryerson, F.J., Tapponnier, P., Finkel, R.C., Mériaux, A.S., Van der Woerd, J., Lasserre, C., Chevalier, M.L., Xiwei, X., Li, H., & King, G.C.P. (2006), Applications of morphochronology to the active tectonics of Tibet, in Siame, L.L., Bourles, D.L., and Brown, E.T. ,eds., Application of Cosmogenic Nuclides to the Study of Earth Surface Processes: The Practice and the Potential. *Geological Society of America Special Paper 415*, 61–86, doi: 10.1130/2006.2415(05)

Seismological bureau of Xinjiang Uygur autonomous region (1997), Instruction of Xinjiang Uygur autonomous region seismotectonic map (1:2000000), Xinjiang.

994 Shen, Z. K., Wang, M., Li, Y., Jackson, D. D., Yin, A., Dong, D., & Fang, P. (2001), Crustal
995 deformation along the Altyn Tagh fault system, western China, from GPS. *Journal of*
996 *Geophysical Research: Solid Earth, 106*(B12), 30607-30621.
997 https://doi:10.1029/2001jb000349.
998 Sobel, E. R., & Dumitru, T. A. (1997), Thrusting and exhumation around the margins of the
999 western Tarim basin during the India-Asia collision. *Journal of Geophysical Research,*
1000 *102(*B3), 5043-5063. https://doi.org/10.1029/96JB03267.
1001 Stewart, N., Gaudemer, Y., Manighetti, I., Serreau, L., Vincendeau, A., Dominguez, S., …
1002 Malavieille, J. (2018), "3D_Fault_Offsets," a Matlab code to automatically measure
1003 lateral and vertical fault offsets in topographic data: Application to San Andreas, Owens
1004 Valley, and Hope faults. *Journal of Geophysical Research, 123*, 815–835.
1005 https://doi.org/10.1002/2017JB014863
1006 Stone, J.O. (2000), Air pressure and cosmogenic isotope production. *Journal of Geophysical*
1007 *Research, 105*(B10), 23753-23759. https://doi:10.1029/2000jb900181.
1008 Tao, Y., Xiong, J., Zhang, H., Chang, H., & Li, L. (2020), Climate-driven formation of fluvial
1009 terraces across the Tibetan Plateau since 200 kya: A review. *Quaternary Science Reviews, 237*,
1010 106303. doi: 10.1016/j.quascirev.2020.106303.
1011 Tapponnier, P., & Molnar, P. (1977), Active faulting and tectonics in China. *Journal of*
1012 *Geophysical Research, 82(*20), 2905-2930. https://doi:10.1029/jb082i020p02905.
1013 Tapponnier, P., Xu, Z., Roger, F., Meyer, B., Arnaud, N., Wittlinger, G., & Yang, J. (2001),
1014 Oblique stepwise rise and growth of the Tibet Plateau. *Science, 294(*5547), 1671-1677.
1015 https://doi:10.1126.science.105978.

1016 Van Buer, N. J., Jagoutz, O., Upadhyay, R., & Guillong, M. (2015), Mid-crustal detachment
1017 beneath western Tibet exhumed where conjugate Karakoram and Longmu–Gozha Co faults
1018 intersect. *Earth and Planetary Science Letters, 413*, 144-157.
1019 https://doi:10.1016/j.epsl.2014.12.053.
1020 Van Der Woerd, J. V., Tapponnier, P., J. Ryerson, F., Mériaux, A.-S., Meyer, B., Gaudemer, Y.,
1021 Finkel, R. C., Caffee, M. W., Guoguan, Z., & Zhiqin, X. (2002), Uniform postglacial slip-
1022 rate along the central 600 km of the Kunlun Fault (Tibet), from 26Al, 10Be, and 14C dating
1023 of riser offsets, and climatic origin of the regional morphology. *Geophysical Journal*
1024 *International, 148(*3), 356-388. https://doi:10.1046/j.1365-246x.2002.01556.x.
1025 Wang, H., & Wright, T. (2012), Satellite geodetic imaging reveals internal deformation of
1026 western Tibet. *Geophysical Research Letters, 39(*7). https://doi:10.1029/2012gl051222.
1027 Wang, M., & Shen, Z. K. (2020), Present□day crustal deformation of continental China derived
1028 from GPS and its tectonic implications. *Journal of Geophysical Research, 125*(2),
1029 e2019JB018774. https://doi:10.1029/2012gl051222.
1030 Wells, D. L., & Coppersmith, K. J. (1994), New empirical relationships among magnitude,
1031 rupture length, rupture width, rupture area, and surface displacement. *Bulletin of the*
1032 *seismological Society of America, 84*(4), 974-1002.
1033 Wen, Y., Xu, C., Liu, Y., & Jiang, G. (2016), Deformation and source parameters of the 2015
1034 Mw 6.5 earthquake in Pishan, western China, from Sentinel-1A and ALOS-2 data. *Remote*
1035 *sensing, 8*(2), 134. https://doi:10.3390/rs8020134.
1036 Whipple, K. X., & Tucker, G. E. (1999), Dynamics of the stream□power river incision model:
1037 Implications for height limits of mountain ranges, landscape response timescales, and

research needs. *Journal of Geophysical Research, 104*(B8), 17661-17674. https://doi:10.1029/1999jb900120.

Wittlinger, G., Vergne, J., Tapponnier, P., Farra, V., Poupinet, G., Jiang, M., Su, H., Herquel, G., & Paul, A. (2004), Teleseismic imaging of subducting lithosphere and Moho offsets beneath western Tibet. *Earth and Planetary Science Letters, 221*(1-4), 117-130.

Wright, T. J., Parsons, B., England, P. C., & Fielding, E. J. (2004), InSAR observations of low slip rates on the major faults of western Tibet. *Science, 305(*5681), 236-239. https://doi:10.1126/science.1096388.

Xu, X., Tan, X., Yu, G., Wu, G., Fang, W., Chen, J. et al. (2013), Normal-and oblique-slip of the 2008 Yutian earthquake: evidence for eastward block motion, northern Tibetan Plateau. *Tectonophysics, 584*, 152-165. https://doi:10.1016/j.tecto.2012.08.007.

Yao, T., Jiao, K., Tian, L., Yang, Z., Shi, W., & Thompson, L.G. (1996), Climatic variations since the Little Ice Age recorded in the Guliya Ice Core. *Science in China*, 39, 6.

Yang, Y., Li, Q., Ai, M., Shi, Z., Yan, J. (1991), Some queries for the Hotan earthquake 1882 and the Yeeryang earthquake 1889 in Xinjiang. *Northeastern Seismological Research*, *7*(1), 87-93. https://doi: 10.13693/j.cnki.cn21-1573.1991.01.014.

Zechar, J. D., & Frankel, K. L. (2009), Incorporating and reporting uncertainties in fault slip rates. *Journal of Geophysical Research, 114*, B12407. https://doi.org/10.1029/2009JB006325.